2012

First principles analysis of lattice dynamics for Fe-based superconductors and entropically-stabilized phases

Steven Edward Hahn
Iowa State University

First principles analysis of lattice dynamics for Fe-based superconductors and entropically-stabilized phases

by

Steven Edward Hahn

A dissertation submitted to the graduate faculty

in partial fulfillment of the requirements for the degree of

DOCTOR OF PHILOSOPHY

Major: Condensed Matter Physics

Program of Study Committee:

Bruce Harmon, Major Professor

Robert McQueeney

Marshall Luban

German Valencia

Richard LeSar

Iowa State University

Ames, Iowa

2012

TABLE OF CONTENTS

LIST OF TABLES

LIST OF FIGURES

ACKNOWLEDGEMENTS

I would like to express my gratitude to everyone who helped me while I have been a graduate student in the Ames Laboratory and Department of Physics and Astronomy at Iowa State University. First, I would like to thank my major professor, Bruce Harmon, for his guidance, patience and encouragement throughout my graduate education. I would like to thank Robert McQueeney for inviting me to participate at the beamline, his guidance with the experimental work and data analysis and in many ways becoming a co-major professor. I would also like to thank Yongbin Lee for introducing me to the software codes and clusters as well as the many meetings and discussions we have had during my graduate career. In addition, I want to thank the members of my program of study committee for their time and effort: Marshall Luban, German Valencia and Richard LeSar. Lastly, I would like to thank my parents, David and Janice Hahn, for encouraging me to go into science and everything they have done to help me achieve this degree and my girlfriend Marissa Nagy for all of her support along this journey.

This work was performed at the Ames Laboratory under contract number DE-AC02-07CH11358 with the U.S. Department of Energy. The document number assigned to this thesis/dissertation is IS-T 3060.

ABSTRACT

Modern *ab initio* calculations are becoming an essential, complementary tool to inelastic x-ray scattering studies, where x-rays are scattered inelastically to resolve meV phonons. Calculations of the inelastic structure factor for any value of **Q** assist in both planning the experiment and analyzing the results. Moreover, differences between the measured data and theoretical calculations help identify important new physics driving the properties of novel correlated systems. We have used such calculations to better and more efficiently measure the phonon dispersion and elastic constants of several iron pnictide superconductors. This dissertation describes calculations and measurements at room temperature in the tetragonal phase of $CaFe_2As_2$ and LaFeAsO. In both cases, spin-polarized calculations imposing the antiferromagnetic order present in the low-temperature orthorhombic phase dramatically improves the agreement between theory and experiment. This is discussed in terms of the strong antiferromagnetic correlations that are known to persist in the tetragonal phase. In addition, we discuss a relatively new approach called self-consistent *ab initio* lattice dynamics (SCAILD), which goes beyond the harmonic approximation to include phonon-phonon interactions and produce a temperature-dependent phonon dispersion. We used this technique to study the HCP to BCC transition in beryllium.

CHAPTER 1. Introduction

Modern *ab initio* calculations are becoming an essential, complementary tool to inelastic x-ray scattering studies, where much higher energy x-rays are scattered inelastically to resolve meV phonons. Calculations of the inelastic structure factor for any value of **Q** assist in both planning the experiment and analyzing the results. Moreover, differences between the measured data and theoretical calculations help identify important new physics driving the properties of novel correlated systems. In this work we have used such calculations to better and more efficiently measure and study the phonon dispersion of several iron pnictide superconductors. In addition, we have used a relatively new approach called self-consistent *ab initio* lattice dynamics (SCAILD), which goes beyond the harmonic approximation to allow for first principles calculations of phonons in entropically stabilized materials.

Chapter 2 provides a brief overview of Density Functional Theory (DFT), the underlying method used for these calculations. First, we discuss the Hohenberg-Kohn theorems that provide the theoretical footing for DFT and the Kohn-Sham equations that map the intractable problem of interacting electrons onto a system of noninteracting particles moving in an effective potential. Lastly, we discuss approximations to the unknown exchange-correlation functional and discuss one common basis set using planewaves to represent the Kohn-Sham wavefunctions and pseudopotentials that reduce the computational demands of these calculations.

Chapter 3 discusses first principles approaches to calculating phonons. We first derive the dynamical matrix and discuss two methods that work on top of DFT to calculate it. The small displacement method is simple to implement on top of any DFT code, but relies on supercells with many atoms in a unit cell. Density Functional Perturbation Theory (DPFT) requires much more human effort to implement, but provides the ability to calculate phonons at any value of **Q** with similar computational effort. Next, we discuss inelastic x-ray scattering

and calculating the dynamical structure factor from these phonon calculations. Lastly, we go through improvements made to our first calculations and how each changes the results.

Chapter 4 motivates our studies of two different subsets of the ferropnictides that have generated great interest due to observed unconventional superconductivity and an interesting phase diagram resembling the cuprate superconductors. Chapters 5 and 6 discuss first principles calculations and inelastic x-ray scattering measurements of phonons at room temperature in the tetragonal phase of $CaFe_2As_2$ and LaFeAsO, respectively. Spin-polarized calculations imposing the antiferromagnetic order present in the low-temperature orthorhombic phase are in better agreement with the experimental results than nonmagnetic calculations. This is discussed in terms of the strong antiferromagnetic correlations that are known to persist in the tetragonal phase. Chapter 5 was published in *Physical Review B* **79** 220511(R) (2009).

Chapter 6 discusses calculations and measurements of c-axis phonons at room temperature in the tetragonal phase of LaFeAsO. Spin-polarized first-principles calculations imposing various types of antiferromagnetic order are in better agreement with the experimental results than nonmagnetic calculations, even though the measurements were made well above the magnetic ordering temperature, T_N. Magneto-structural effects similar to those observed in the AFe_2As_2 materials are confirmed present in LaFeAsO. On-site Fe and As force constants show significant softening compared to nonmagnetic calculations, however an investigation of the real-space force constants associates the magnetoelastic coupling with a complex renormalization instead of softening of a specific pairwise force. Chapter 5 has been submitted to *Physical Review B*.

Lastly, Chapter 6 will briefly discuss a relatively new approach called self-consistent *ab initio* lattice dynamics (SCAILD), which goes beyond the harmonic approximation to include phonon-phonon interactions and produces a temperature-dependent phonon dispersion. We used this technique to study the HCP to BCC transition in beryllium. We begin by studying the low-temperature HCP structure and confirm that calculations of phonons and elastic constants using the small displacement method are in good agreement with experiment. In the BCC structure however, imaginary frequencies appear near the N-point. While not surprising considering the structural transition with temperature, such calculations poorly describe phonons in the BCC structure. Using the SCAILD method, we show that phonon-phonon

interactions stabilize the N-point phonon mode and stiffen phonon frequencies at the P-point. Lastly, we use the Christhoffel Equation to estimate elastic constants in the HCP and BCC phases and compare the latter with elastic constants derived from properties of the HCP phase.

CHAPTER 2. Electronic Structure Calculations

First principles calculations start with the established laws of physics and only a minimal number of input parameters including the atomic types and positions. No additional experimental data is required. With such minimal a priori knowledge, these calculations are a powerful tool for predicting new materials and their properties and explaining and supporting experiments. This chapter introduces one first principles method called Density Functional Theory for which Walter Kohn was awarded the Nobel prize in Chemistry in 1998. A full review of this 47 year old method would be quite long and beyond the scope of this dissertation, and the reader is directed to the literature. Yongbin Lee's dissertation[8] and a talk given by Richard Hennig at the 2012 Pan-American Advanced Studies Institute in Santiago, Chile [9] and references therein were very helpful while writing this chapter.

2.1 Born-Oppenheimer Approximation

Calculating properties of materials begins with the Schrödinger equation,

$$\hat{H}\Psi = E\Psi\left(r_1, r_2, ..., r_N\right), \tag{2.1}$$

where $\hat{H}$ is the Hamiltonian operator describing the kinetic and potential energy of the system and $\Psi\left(r_1, r_2, ..., r_N\right)$ is the quantum mechanical wavefunction that depends on every electron and nuclei in the material. This equation, however, can only be solved exactly and directly for the smallest systems. With bulk materials containing on order of 10^{23} atoms, approximations need to be made. In 1929, Paul Dirac wrote that "the underlying physical laws necessary for the mathematical theory of a large part of physics and the whole of chemistry are thus completely known, and the difficulty is only that the exact application of these laws

leads to equations much too complicated to be soluble. It therefore becomes desirable that approximate practical methods of applying quantum mechanics should be developed, which can lead to an explanation of the main features of complex atomic systems without too much computation"[10]. The history of condensed matter contains incremental leaps in the accuracy of these approximate solutions.

One of the first leaps made in electronic structure calculations is the Born-Oppenheimer adiabatic approximation. The nuclei in the system are thousands of times heavier than the electrons ($m_p/m_e \approx 1837$) and consequently for their motion relative to the electrons, one can assume the nuclei are fixed. Consequently, in this approximation the kinetic energy of the nuclei is zero and the term describing nuclei-nuclei interactions becomes a constant term which does not effect the equations of motion. The Hamiltonian describing the electrons among the stationary nuclei is

$$H = -\left(\frac{\hbar^2}{2m}\right)\sum_i \nabla_i^2 + \frac{1}{2}\sum_{i\neq j}\frac{e^2}{|r_i - r_j|} - \sum_{i,I}\frac{e^2 Z^I}{|r_i - R_I|} \tag{2.2}$$

In this expression, m and r_i are the electron mass and position, R_I is the position of each nuclei, and eZ^I gives the charge of each nuclei. The first term gives the quantum kinetic energy of the electrons. The second term describes electron-electron interactions, and the third term describes electrostatic electron-nuclei interactions. The next section will discuss an approach to solving this equation for the ground state of the electron system, called density functional theory. The following sections will discuss calculating phonons, or vibrations of the nuclei.

2.2 Density Functional Theory

2.2.1 Hohenberg-Kohn Theorems

In 1964 Hohenberg and Kohn[11] published two important theorems that have become the foundations of density functional theory.

First Hohenberg-Kohn Theorem: The external potential $V_{ext}(r)$ is determined uniquely, within a trivial additive constant, by the electron density $n(r)$

The Hamiltonian of a quantum system is fixed by the external potential and determines the electron density and all ground state properties. This theorem proves that the reverse is also true. The external potential can be determined from the ground state electron density $n(\mathbf{r})$.

Second Hohenberg-Kohn Theorem: The ground state energy can be obtained variationally. The density that minimizes the total energy is the exact ground state density.

Alternatively,

$$E\left[n(\mathbf{r})\right] = T\left[n(\mathbf{r})\right] + V\left[n(\mathbf{r})\right] + \int v_{ext}(\mathbf{r})n(\mathbf{r})d^3r \geq E_0 \tag{2.3}$$

where $T\left[n(\mathbf{r})\right]$ is the interacting kinetic energy functional and $V\left[n(\mathbf{r})\right]$ is the Coulomb potential functional for the interacting system. Consquently the ground state energy and electron density can be found by minimizing a functional of the three-dimentional electron density. While the Hohenberg-Kohn theorems are extremely powerful, they do not offer a way of computing the ground-state density of a system in practice. The major problem remaining is determining the functional $T\left[n(\mathbf{r})\right] + V\left[n(\mathbf{r})\right]$.

2.2.2 Kohn-Sham Equations

Shortly after Hohenberg and Kohn, Kohn and Sham[12, 13] showed how to map the difficult interacting many-body problem onto a non-interacting system that can be solved completely and easily. In a non-interacting system the kinetic energy is well defined

$$T_S\left[n(\mathbf{r})\right] = -\frac{1}{2}\sum_{i=1}^{N}\int \varphi_i^*(\mathbf{r})\nabla^2\varphi_i(\mathbf{r}) \tag{2.4}$$

The Hartree energy is the classical Coulomb energy for a charge distribution

$$E_H\left[n(\mathbf{r})\right] = \frac{1}{2}\int\int \frac{n(\mathbf{r})n(\mathbf{r}')}{|\mathbf{r}-\mathbf{r}'|}d^3\mathbf{r}d^3\mathbf{r}' \tag{2.5}$$

We then add and subtract both of these quantities to the energy functional in Eqn. 2.3.

$$E\left[n\right] = T_s\left[n\right] + E_H\left[n\right] + \left(T\left[n\right] - T_s\left[n\right] - E_H\left[n\right] + V\left[n\right]\right) + \int v_{ext}(\mathbf{r})n(\mathbf{r})d^3r \tag{2.6}$$

$$E\left[n\right] = T_s\left[n\right] + E_H\left[n\right] + E_{xc}\left[n\right] + \int v_{ext}(\mathbf{r})n(\mathbf{r})d^3r \tag{2.7}$$

where we have defined $E_{xc}[n] \equiv T[n] - T_s[n] - E_H[n] + V[n]$ to be the exchange and correlation energies of an interacting system with density $n(\mathbf{r})$. While no simple exact expression for $E_{xc}[n]$ exists, successful approximations are discussed further in section 2.3. The stationary property of the energy functional subject to the constraint

$$\int \delta n(\mathbf{r}) = 0 \tag{2.8}$$

leads to the equation

$$\int \delta n(\mathbf{r}) \left(\frac{\delta T_s[n]}{\delta n(\mathbf{r}')} + V_H(\mathbf{r}) + V_{xc}(\mathbf{r}) + v(\mathbf{r}) \right) d^3r = 0 \tag{2.9}$$

where

$$V_H = \int \frac{n(\mathbf{r})}{|\mathbf{r} - \mathbf{r}'|} d^3r' \tag{2.10}$$

and

$$V_{xc}(\mathbf{r}) = \frac{\delta E_{xc}[n]}{\delta n(\mathbf{r})} \tag{2.11}$$

The resulting Kohn-Sham equations resemble the single particle Schrödinger equation

$$\left(-\frac{1}{2}\nabla^2 + V_H(\mathbf{r}) + V_{xc}(\mathbf{r}) + v(\mathbf{r}) \right) \varphi_i(\mathbf{r}) = \epsilon_i \varphi_i(\mathbf{r}) \tag{2.12}$$

The ground-state charge density is given by

$$n(\mathbf{r}) = \sum_{i=1}^{N} |\varphi_i(\mathbf{r})|^2 \tag{2.13}$$

and identical to the charge density of the interacting system.

The orbital energies are related to the total energy by

$$E_{TOT} = \sum_{i=1}^{N} \epsilon_i - V_H[n(\mathbf{r})] + E_{xc}[n(\mathbf{r})] - \int n(\mathbf{r}) v_{xc}(\mathbf{r}) d^3r \tag{2.14}$$

While the eigenvalues of the Kohn-Sham equation are not energies of electrons, they are often successfully interpreted as such.

The most common computational approach to solving the Kohn-Sham equations is to construct a basis set to represent the Kohn-Sham orbitals

$$\varphi_i(\mathbf{r}) = \sum_j c_{ij}\phi(\mathbf{r}) \tag{2.15}$$

where $\phi(\mathbf{r})$ are the basis functions and c_{ij} are expansion coefficients. Finding solutions amounts to determining the coefficients for the occupied orbitals that minimize the total energy using the following procedure:

1. Guess an initial electron density.

2. Construct the Kohn-Sham Hamiltonian and solve the eigenvalue equation at each $\mathbf{k}$ point in the irreducible Brillouin zone.

3. Fill states with N electrons and calculate the new charge density.

4. Mix the old and new charge density for the next step.

5. Calculate the new Kohn-Sham Hamiltonian from the density in step 4.

6. Iterate until the solution reaches self-consistency (changes in the total energy or charge density are below a specified threshold)

2.3 Exchange Correlation Potential

So far only the Born-Oppenheimer approximation has been made, meaning the Kohn-Sham equations are exact for the ground state system. Density Functional Theory has rewritten the simple but intractable Schrödinger equation into a separable equation with an unknown functional! While the exact form of the exchange correlation functional is not known, a number of successful approximations have been made. For a weakly inhomogenous gas where $n(\mathbf{r})$ varies slowly, Kohn and Sham suggested writing the exchange-correlation potential in the form

$$E_{xc}\left[n(\mathbf{r})\right] = \int \epsilon_{xc}(n(\mathbf{r}))n(\mathbf{r})d^3r \tag{2.16}$$

where $\epsilon_{xc} = \epsilon_x + \epsilon_c$. The exchange energy density, ϵ_x, is obtained from the Hartree-Fock approximation for a uniform system

$$\epsilon_x(n(\mathbf{r})) = -\frac{3}{4}\, e^2 \left(\frac{3}{\pi}\right)^{1/3} [n(\mathbf{r})]^{1/3} \tag{2.17}$$

The correlation energy density, ϵ_c is only known in the high and low density limits. In between these limits, fits are made to quantum monte carlo simulations of a uniform electron gas by Ceperley and Alder[14]. Many different parameterizations are available such as those of Hedin and Lundqvist[15], von Barth and Hedin[16], Perdew and Zunger[17], Voskoi, Wilk and Nusair[18], Teter and Pade[19], and Perdew and Wang[20]. Given that all of these parameterizations are fit to the same calculations, differences between them are small.

A common extension called the generalized gradient approximation (GGA) is to also introduce the gradients of the density into the functional

$$E_{xc}\left[n(\mathbf{r})\right] = \int n(\mathbf{r})\epsilon_{xc}(n, \nabla n) d^3\mathbf{r} \tag{2.18}$$

Initial attempts included the gradient expansion approximations which systematically added gradient corrections to the local density approximation[21, 22]. GGA functionals of this form were often worse than LDA and violate sum-rules. Modern GGA functionals are more general functions of $n(\mathbf{r})$ and $\nabla n(\mathbf{r})$ that satisfy a number of exact constraints. Examples include those by Perdew and Wang[23] and Perdew, Burke and Enzerhof[24], The latter functional was used in our studies of $CaFe_2As_2$ and LaFeAsO. In practice, GGA functionals do not always outperform LDA functionals and show more variation between parameterizations. The choice of functional is often decided by comparing agreement between calculations and experimental data.

2.4 Plane Waves and Pseudopotentials

Planewaves form a convenient basis set for periodic crystals. They explicitly satisfy Bloch's theorem, which states that the wavefunction for a system can be written as the product of a plane wave and a function with the same periodicity as the unit cell.

$$\varphi_k(\mathbf{r}) = e^{i\mathbf{k}\cdot\mathbf{r}} \sum_G C_G(\mathbf{k}) e^{i\mathbf{G}\cdot\mathbf{r}} \tag{2.19}$$

In addition, planewaves are the solution for an empty lattice. A small periodic perturbation leads to mixtures of planewaves with similar energies. The basis set can be cut off by a single parameter E_{cut}, which is the maximum kinetic energy of any planewave in the expansion.

$$\frac{1}{2}(\mathbf{k}+\mathbf{G})^2 \leq E_{cut} \tag{2.20}$$

Unfortunately, solids contain electrons and nuclei interacting strongly via a $-Ze^2/r$ Coulomb potential. These electrons have wavefunctions that oscillate rapidly near the nuclei and quickly drop off to zero further away. In addition, the requirement that states with different quantum numbers must be orthogonal leads to a number of nodes in valence wavefunctions near the atomic nuclei. Expanding these wavefunctions in terms of plane waves requires an extremely high energy cutoff to accurately represent these core electrons. Such a calculation would be incredibly slow and inefficient.

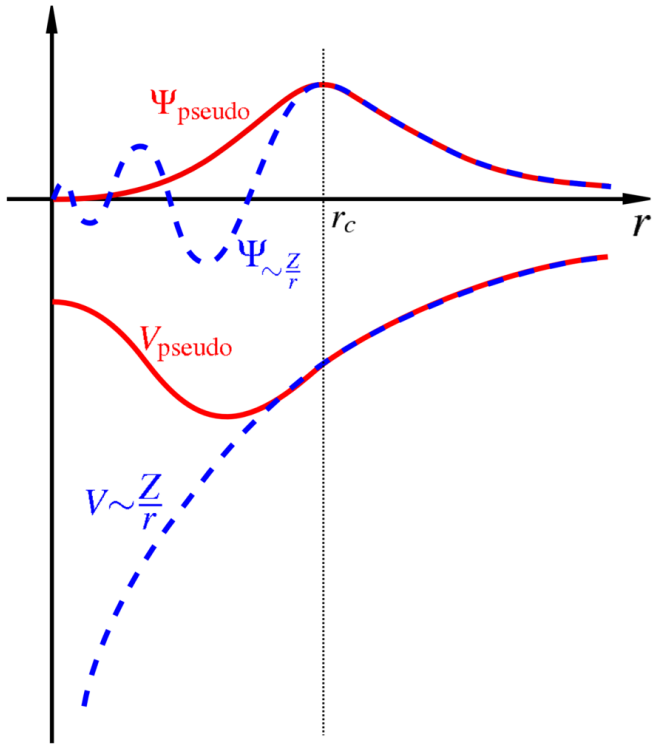

Figure 2.1 Comparison of the Coulomb potential and its correpesonding pseudopotential. Near the nucleus the pseudopotential is much weaker and the wavefunction smoother. Beyond a certain radius, r_c, both wavefunctions and potentials match.[5]

Fortunately these core electrons are strongly bound and are essentially fixed compared to the motions of the valence electrons and do not contribute to bonding. In the peudopotential approximation, shown in Fig. 2.1, the strong core potential is replaced by a peudopotential that mimics the potential from the nuclei and core electrons. Outside a selected core radius from each atom, the ground state wavefunctions of the pseudopotential are equal to the all electron wavefunctions. Often these pseudo-wavefunctions are quite smooth and well-represented by a much smaller number of planewaves. Many sophisticated and effective approaches to generating pseudopotentials have evolved. See, for example, Ref.[25] for a discussion of the formalism and pseudopotential generation. In practice, highly transferrable pseudopotentials are often distributed with plane wave codes and the user's job reduces to verifying the validity of the pseudopotential to the particular problem, either by testing against experimental data or from a separate all-electron calculation.

CHAPTER 3. Calculating Phonons From First Principles

In this chapter we relax the assumption that the nuclei are fixed and discuss first principles approaches to calculating phonons. We first derive the dynamical matrix and discuss two methods that work on top of DFT to calculate it, the small displacement method and density functional perturbation theory (DPFT). Next, we briefly discuss inelastic x-ray scattering and calculating the dynamical structure factor to compare with experiment. Lastly, we go through several improvements made since our first calculations of the dynamical structure factor and how each changes the results.

3.1 Dynamical Matrix

Phonon calculations are used to obtain the dynamical matrix, which we derive in this section. Much of this section is covered in Ref.[26] and a talk by Ronald Cohen at the 2007 Summer School on Computational Materials Science at the University of Illinois at Urbana-Champaign[27]. In general, the position of each atom, $\mathbf{x}_{ld}$, is described in terms of a Bravais lattice point $\mathbf{x}_l$ and a basis vector, $\mathbf{x}_d$. Both are described in terms of the lattice vectors $\mathbf{a_i}$. In Eqn. 3.2, l_i are integers, and in Eqn. 3.3 λ_i are decimals or fractions, typically chosen between 0 and 1.

$$\mathbf{x}_{ld} = \mathbf{x}_l + \mathbf{x}_d \tag{3.1}$$

$$\mathbf{x}_l = l_1\mathbf{a_1} + l_2\mathbf{a_2} + l_3\mathbf{a_3} \tag{3.2}$$

$$\mathbf{x}_d = \lambda_1\mathbf{a_1} + \lambda_2\mathbf{a_2} + \lambda_3\mathbf{a_3} \tag{3.3}$$

Let us allow each atom to be displaced by an amount $\mathbf{u}_{ld}$ from its equilibrium position, $\mathbf{x}_{ld}$.

$$\mathbf{R}_{ld} = \mathbf{x}_{ld} + \mathbf{u}_{ld} \tag{3.4}$$

For small values of $\mathbf{u}_{ld}$, we can expand the total energy in a Taylor series though second order.

$$E = E_o + \sum_{l,d,\alpha} \frac{\partial E}{\partial u_{ld\alpha}} u_{ld\alpha} + \frac{1}{2} \sum_{\alpha,\beta,l,d,l',d'} \frac{\partial^2 E}{\partial u_{ld\alpha} \partial u_{l'd'\beta}} u_{ld\alpha} u_{l'd'\beta} \tag{3.5}$$

In this equation α and β are the Cartesian coordinates x, y and z. Plugging this into the equation of motion, $\mathbf{F}$=m$\mathbf{a}$

$$m_d \frac{\partial^2 u_{ld\alpha}}{\partial t^2} = -\frac{\partial E}{\partial u_{ld\alpha}} \tag{3.6}$$

The first term of the Taylor series is a constant and does not enter into the equation of motion. In the second (linear) term, all forces on the atoms must be zero at the equilibrium positions. Therefore, $\frac{\partial E}{\partial u_{ld\alpha}} = 0$ for all atoms in all directions. Consequently, the first nonzero term is the third (quadratic) term in Eqn. 3.5.

The final equation of motion is

$$m_d \frac{\partial^2 u_{ld\alpha}}{\partial t^2} = -\sum_{l'd'\beta} \frac{\partial^2 E}{\partial u_{ld\alpha} \partial u_{l'd'\beta}} u_{l'd'\beta} \tag{3.7}$$

To solve this equation we consider solutions in the form

$$u_{ld\alpha} = \frac{1}{\sqrt{m_d}} \epsilon_{\alpha d} e^{i\mathbf{q}\cdot\mathbf{x}_{ld} - i\omega t} \tag{3.8}$$

substituting this into the equation of motion gives the eigenvalue equation

$$\omega^2 \epsilon_{\alpha d} = \sum_{d',\beta} D_{\alpha d \beta d'}(\mathbf{Q}) \epsilon_{\beta d'} \tag{3.9}$$

where $D_{\alpha d \beta d'}(\mathbf{Q})$ is the dynamical matrix given by

$$D_{\alpha,d,\beta,d'}(\mathbf{Q}) = \frac{1}{\sqrt{m_d, m_{d'}}} \sum_{l'} \frac{\partial^2 E}{\partial u_{ld\alpha} \partial u_{l'd'\beta}} e^{-i\mathbf{Q}\cdot\mathbf{x}_{ll'}} \tag{3.10}$$

In the final expression, only the difference between $\mathbf{x}_{ll'} = \mathbf{x}_l - \mathbf{x}_{l'}$ matters. It is also useful to note that the dynamical matrix is Hermitian and there are 3N solutions to this eigenvalue equation. At this point the problem becomes finding the second derivative of the energy. With that information, one can calculate the dynamical matrix for any value of $\mathbf{Q}$ and solve it to find the phonon frequencies and eigenvectors. Next we consider two strategies for finding the derivatives of the energy: the small displacement method and density functional perturbation theory.

3.2 Small Displacement Method

The second derivatives of the energy can be approximated by calculating changes in the forces on all atoms from a small displacement of another.

$$\frac{\partial^2 E}{\partial u_{\alpha ld} \partial u_{\beta l'd'}} = -\frac{\partial F_{\alpha ld}}{\partial u_{\beta l'd'}} \approx -\frac{\Delta F_{\alpha ld}}{u_{\beta l'd'}} \tag{3.11}$$

In principle this requires 3N displacements, however symmetry can be exploited to reduce this number substantially[28]. For example the phonon calculations of BCC beryllium only require one displacement and phonon calculations of HCP beryllium only require two displacements. DFT calculations where one atom is moved are used to calculate Hellmann-Feynman forces on all atoms. The Hellmann-Feynman theorem[29, 30] states that the first derivative of the eigenvalues of a Hamiltonian is equal to the expectation value of the derivative of the Hamiltonian.

$$\mathbf{F}_I = -\frac{\partial E(\mathbf{R})}{\partial \mathbf{R}_I} = -\left\langle \Psi(\mathbf{R}) \left| \frac{\partial H(\mathbf{R})}{\partial \mathbf{R}_I} \right| \Psi(\mathbf{R}) \right\rangle \tag{3.12}$$

Two terms in the Hamiltonian depend on the atomic positions. Taking the derivative with respect to the atom at position $\mathbf{R_I}$

$$\mathbf{F}_I = -\int n_{\mathbf{R}}(\mathbf{r}) \frac{\partial V_{\mathbf{R}}(\mathbf{r})}{\partial \mathbf{R}_I} d^3 r - \frac{\partial E_N(\mathbf{R})}{\partial \mathbf{R}_I} \tag{3.13}$$

where $V_{\mathbf{R}}(\mathbf{r})$ is the electron-nucleus interaction given in the third term of Eqn. 2.2 and $E_N(\mathbf{R})$ is the electrostatic interaction between different nuclei

$$E_N(\mathbf{R}) = \frac{e^2}{2} \sum_{I \neq J} \frac{Z_I Z_J}{|\mathbf{R}_I - \mathbf{R}_J|} \tag{3.14}$$

Only the ground state charge density is required to calculate such forces and consequently forces are implemented by all popular DFT codes. It should be noted that supercells containing multiple copies of the primitive cell are required for these calculations. The displaced atom is repeated in each supercell, leading to an expression that only approaches the Dynamical matrix as the supercell increases in size. Therefore, the supercell should also be large enough so that forces on the most distant atoms approach zero and the displaced atoms in neighboring supercells do not interact. Unfortunately, the use of supercells is the largest limitation of this method. The computer time required by DFT codes scales as the number of electrons cubed, meaning that large supercells quickly reach the limits of modern computers and the patience of the user. Fortunately, there is another method that, while more difficult to implement, avoids supercells and consequently can calculate phonons at any value of $\mathbf{Q}$ with similar computational effort.

3.3 Density Functional Perturbation Theory

Density Functional Perturbation Theory (DFPT) provides an alternative procedure for calculating phonons and other response functions. Differentiating Eqn. 3.13 with respect to the atom at position $\mathbf{R}_J$

$$\frac{\partial^2 E(\mathbf{R})}{\partial \mathbf{R}_I \partial \mathbf{R}_J} = -\frac{\partial \mathbf{F}_I}{\partial \mathbf{R}_J} \tag{3.15}$$

$$= \int \frac{n_{\mathbf{R}}(\mathbf{r})}{\partial \mathbf{R}_J} \frac{\partial V_{\mathbf{R}}(\mathbf{r})}{\partial \mathbf{R}_I} d^3r + \int n_{\mathbf{R}}(\mathbf{r}) \frac{\partial^2 V_{\mathbf{R}}(\mathbf{r})}{\partial \mathbf{R}_I \partial \mathbf{R}_J} d^3r + \frac{\partial^2 E_N(\mathbf{R})}{\partial \mathbf{R}_I \partial \mathbf{R}_J} \tag{3.16}$$

Calculating the second derivative of the energy requires both the ground state electron density $n(\mathbf{r})$ as well as the linear response to the displacement of a nucleus $\frac{n_{\mathbf{R}}(\mathbf{r})}{\partial \mathbf{R}_J}$. Fortunately, Eqns. 3.17, 3.19 and 3.20 form a set of self-consistent equations completely analogous to the Kohn-Sham equations discussed earlier. Linearizing Eqn. 2.13 leads to[30]

$$\Delta n(\mathbf{r}) = 4Re\sum_{n=1}^{N/2}\varphi^{0*}(\mathbf{r})\Delta\varphi(\mathbf{r}) \tag{3.17}$$

where the finite-difference operator Δ^{R_I} is defined as

$$\Delta^{\mathbf{R}_I}F = \sum_i \frac{\partial F}{\partial \mathbf{R}_I}\Delta\mathbf{R}_I \tag{3.18}$$

and the superscript omitted in the previous expressions. The correction to the self-consistent potential is

$$\Delta V\left(\mathbf{r}\right) = \Delta V_{ext}(\mathbf{r}) + e^2\int\frac{\Delta n(\mathbf{r}')}{|\mathbf{r}-\mathbf{r}'|}d^3r' + \left.\frac{dv_{xc}}{dn}\right|_{n=n(\mathbf{r})}\Delta n(\mathbf{r}) \tag{3.19}$$

Lastly, the variation to the Kohn-Sham orbitals can be obtained via first-order perturbation theory. This is also known as the Sternheimer equation[31].

$$(H-\epsilon_n)\left|\,\Delta\varphi_n\,\right\rangle = -(\Delta V - \Delta\epsilon_n\left|\,\varphi_n^0\,\right\rangle \tag{3.20}$$

Where $\Delta\epsilon_n = \left\langle\,\varphi_n\,\right|\Delta V\left|\,\varphi_n\,\right\rangle$ is the variation in the Kohn-Sham eigenvalue.

One of the greatest advantages of DFPT is that the responses to perturbations of different wavelengths are decoupled. If one considers $\Delta n(\mathbf{q}+\mathbf{G})$ instead of $\Delta n(\mathbf{r})$ and decomposes the perturbing potential into Fourier components, one can carry out the self-consistent process using only functions periodic with the lattice. Consequently, phonons can be calculated at any **Q**-vector with a similar numerical workload. To obtain the full dispersion, derivatives of the energy and wavefunctions are calculated on a grid of **q**-points. The Fourier transform is taken to obtain the real space force constants, which for a fine enough mesh can be used to accurately determine phonons at any value of **Q**.

3.4 Inelastic X-ray Scattering

Inelastic x-ray scattering has several advantages over inelastic neutron scattering. The beam can be easily focused to approximately 100 microns, permitting measurements on very small samples. The energy resolution is independent of the energy transfer and there is very low

background in IXS data. In addition, differences between the x-ray form factor and neutron cross-section may be advantageous depending on the chemical composition[32]. Studies of $CaFe_2As_2$ were performed at Sector 3-ID-C of the Advanced Photon Source at Argonne National Laboratory, shown in Fig. 3.1. The incident energy is 21.66keV. Detector arm is 6m and the analyzers are 10cm across, which is important determining finite Q-resolution. Studies of LaFeAsO were performed at sector 30 of the Advanced Photon Source at Argonne National Laboratory[33, 34], shown in Fig. 3.2. The incident energy is 23.71keV. Detector arm is 9m and the analyzers are 10cm across. The longer arm allows for higher resolution in $\mathbf{Q}$ though lower intensity. The larger allowable scattering angle in 2θ allows for measurements in a larger portion of reciprocal space, potentially where higher intensity is available. Other inelastic x-ray scattering instruments include beamline ID16 at the ESRF in Grenoble, France, and beamline BL35XU at SPring-8 in Kansai, Japan[35].

Corrections are made for changes in the incident intensity and any drift in the incident energy. Multiple scans are taken over a shorter time interval and then added. Afterwards, the scans are fit to several peaks using a pseudo-Voigt line profile. The normalized pseudo-Voigt function is given in eq. 3.21, where $f_G(x;\Gamma)$ and $f_L(x;\Gamma)$ are normalized Gaussian and Lorentzian functions respectively. The mixing parameter η and resolution full-width-at-half-maximum (FWHM) Γ were determined from fits to the elastic scattering width of Plexiglass for each detector, shown in Fig.3.3. The fit parameters for sector 3 are $\eta = 0.39$ and $\Gamma = 2.38$ meV. For sector 30, the fit parameters are $\eta = 0.74$ and $\Gamma = 1.44$ meV. Sometimes it is necessary to include the FWHM as a fit parameter. Finite Q resolution broadens excitations with significant dispersion, however large deviations from the values above may indicate intrinsic broadening and therefore lifetime effects.

$$f_{pV} = (1-\eta) f_G(x;\Gamma) + \eta f_L(x;\Gamma) \tag{3.21}$$

Fig. 3.4 shows a constant-Q energy scan in LaFeAsO at Q=(0.0,0.0,8.3) and Q=(0.0,0.0,8.5) as well as fits to the experimental data. When the Stokes (material absorbs energy) and Anti-Stokes (material releases energy) peaks are present, detailed balance can be used to fit both excitations. The intensity of these two peaks are related to each other by Eqn. 3.22. This

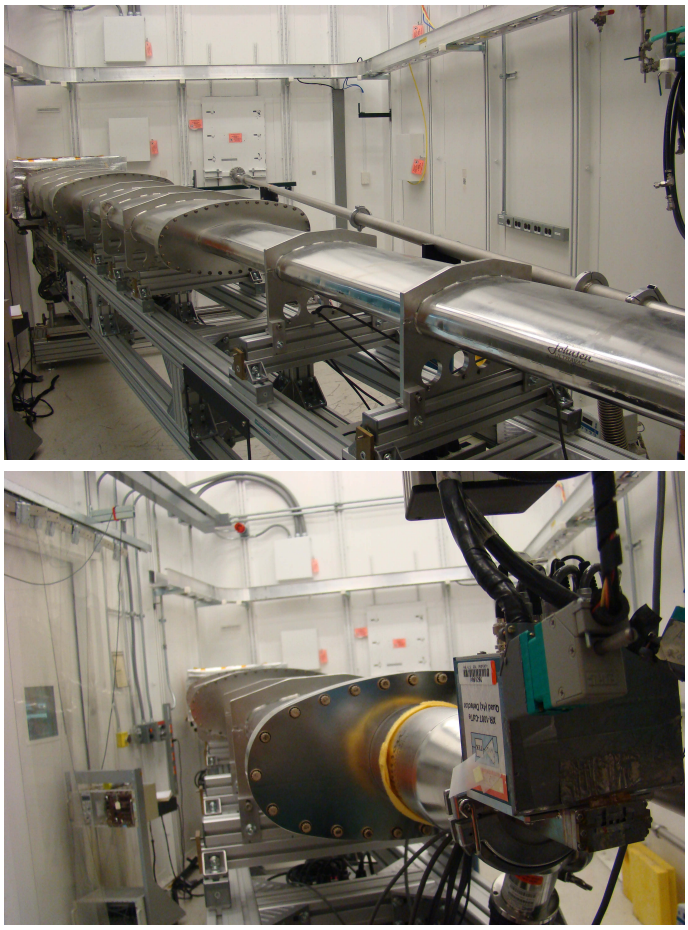

Figure 3.1 Images of sector 3-ID-C of the Advanced Photon Source at Argonne National Laboratory. The top image shows the arm which is moved to adjust 2θ. At the end are four analyzers, allowing for multiple positions in reciprocal space to be measured at once. The lower figure is taken next to the four-circle goniometer (not shown) and shows the detector which measures the back-scattered beam.

is especially useful for fitting acoustic modes near the zone center, which are close to and sometimes hidden by the "tail" from elastic scattering.

$$\frac{1+n_j\left(\mathbf{q}\right)}{n_j\left(\mathbf{q}\right)}=e^{\frac{\hbar\omega}{k_bT}} \tag{3.22}$$

3.4.1 Dynamical Structure Factor

In this section we outline the derivation of the dynamical structure factor which is proportional to the phonon cross section. More detail specific to inelastic x-ray scattering is given

Figure 3.2 Images of sector 30-ID-C of the Advanced Photon Source at Argonne National Laboratory. The top image shows the arm which is moved to adjust 2θ. At the end are nine analyzers, allowing for multiple positions in reciprocal space to be measured at once. The lower figure is taken from the other side of the room and shows the KB Mirror system and four-circle goniometer.

in Refs. [32, 35] as well as books on inelastic neutron scattering such as Refs. [36, 37]. It is most convenient to express the scattering cross section in terms of the product of the probe-sample interaction and the correlation function $S(\mathbf{Q},\omega)$ derived by Van Hove[38] in the Born approximation

$$\frac{d^2\sigma}{d\Omega dE} = \left(\frac{d\sigma}{d\Omega}\right)_0 S(\mathbf{Q},\omega) \tag{3.23}$$

The first term is

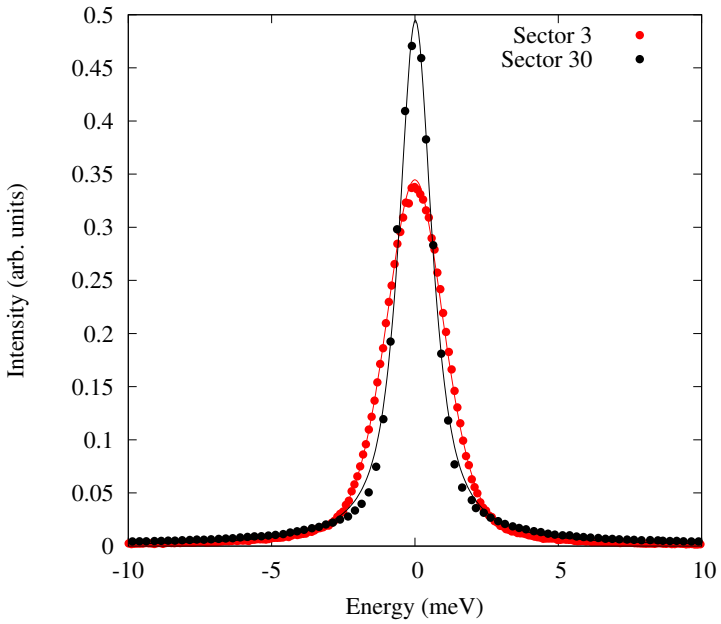

Figure 3.3 Fits to a Plexiglas sample used to determine the energy resolution and peak shape for measurements at HERIX experiments at sectors 3 and 30 at the Advanced Photon Source, Argonne National Laboratory. The intensity was fixed so that the integrated area is equal to one

$$\left(\frac{d\sigma}{d\Omega}\right)_0 = \frac{k_f}{k_i} r_e^2 \left|\epsilon_i \cdot \epsilon_f\right|^2 \tag{3.24}$$

Where $r_e = \frac{e^2}{m_e c^2} = 2.818\text{fm}$ is the classical electron radius. k_f and k_i are the photon momentum and $\frac{k_f}{k_i} \approx 1$ as the photon energy is six or seven orders of magnitude larger than the phonon energy. For nonresonant scattering the photon polarization ϵ_f and ϵ_i is an uninteresting scaling factor.

$$S\left(\mathbf{Q},\omega\right) = \frac{1}{2\pi\hbar N}\int_{-\infty}^{\infty} dt e^{-i\omega t} \sum_{ldl'd'} f_d\left(\mathbf{Q}\right) f_{d'}\left(\mathbf{Q}\right) Y_{ldl'd'}\left(\mathbf{Q},t\right) \tag{3.25}$$

where

$$Y_{ldl'd'} = \left\langle e^{-i\mathbf{Q}\cdot\hat{\mathbf{R}}_{\mathbf{ld}}} e^{i\mathbf{Q}\cdot\hat{\mathbf{R}}_{\mathbf{l'd'}}(\mathbf{t})} \right\rangle \tag{3.26}$$

For non-Bravais lattices like the iron pnictide superconductors, the position vector of an atom is defined in Eqn. 3.3. Using this definition, the correlation function becomes

$$\left\langle e^{-i\mathbf{Q}\cdot\hat{\mathbf{R}}_{\mathbf{ld}}} e^{i\mathbf{Q}\cdot\hat{\mathbf{R}}_{\mathbf{l'd'}}(\mathbf{t})} \right\rangle = e^{i\mathbf{Q}\cdot(\mathbf{x}_{\mathbf{l'd'}}-\mathbf{x}_{\mathbf{ld}})} \times \left\langle e^{-i\mathbf{Q}\cdot\hat{\mathbf{u}}_{\mathbf{ld}}} e^{i\mathbf{Q}\cdot\hat{\mathbf{u}}_{\mathbf{l'd'}}} \right\rangle \tag{3.27}$$

Using the identity $\left\langle e^{\hat{A}} e^{\hat{B}} \right\rangle = e^{\frac{1}{2}\langle \hat{A}^2+\hat{B}^2+2\hat{A}\hat{B}\rangle}$ the right-hand side can be rewritten as

$$e^{-W_d} e^{-W_{d'}} e^{\langle \mathbf{Q}\cdot\hat{\mathbf{u}}_{\mathbf{ld}}\mathbf{Q}\cdot\hat{\mathbf{u}}_{\mathbf{l'd'}}\rangle} \tag{3.28}$$

where W_d is the Debye-Waller factor, given in 3.35 and discussed later in this chapter. Lastly, the final exponential can be expanded in a Taylor series.

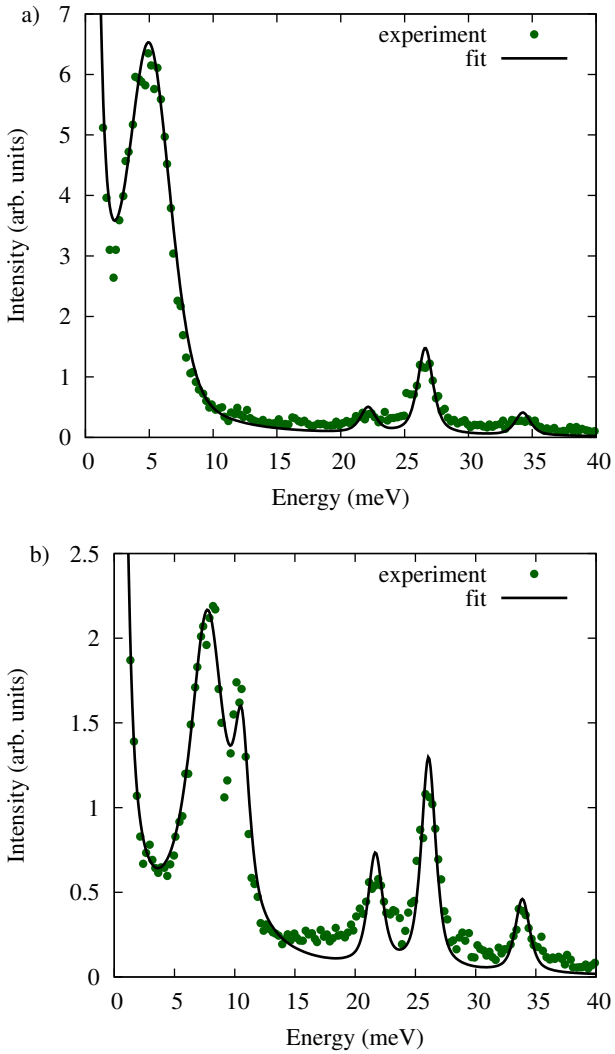

Figure 3.4 (color online) Energy scan at constant-Q at a) $Q = (0.0, 0, 8.3)$ and b) $Q = (0.0, 0, 8.5)$ measured at room temperature on LaFeAsO. Experimental data are given by solid green points. The black line is fit using a pseudo-Voigt function.

$$e^{\left\langle \hat{A}\hat{B}\right\rangle} = 1 + \left\langle \hat{A}\hat{B}\right\rangle + O\left(\left\langle \hat{A}\hat{B}\right\rangle^2\right) \tag{3.29}$$

The first term represents the intensity of elastic scattering at the zone center. The second term represents inelastic one-phonon scattering. Higher order terms represents multi-phonon scattering, and are ignored in our calculations.

A final expression for the Dynamical Structure Factor is given in Eqn. 3.30. In these equations, $W_d(\mathbf{Q})$ is the Debye-Waller factor, $n_j(\mathbf{q})$ is the Bose-Einstein distribution, $f_d(\mathbf{Q})$ is the x-ray form factor, M_d is the mass of atom d and $\sigma^j_{\mathbf{d}}(\mathbf{q})$ is the eigenvector corresponding to the motion of atom d in the j^{th} phonon branch. Instead of making a separate calculation of the phonon eigenvector at $\mathbf{q}$, one can use the complex conjugate of the phonon eigenvector at $\mathbf{Q}$, or $\sigma^{\mathbf{j}}_{\mathbf{d}}(\mathbf{q}) = \left(\sigma^{\mathbf{j}}_{\mathbf{d}}(\mathbf{Q})\right)^*$

$$S_j(\mathbf{Q},\omega) = \frac{\left|H^j_{\mathbf{q}}(\mathbf{Q})\right|^2}{2\omega_j(\mathbf{q})}\left(\left(1+n_j(\mathbf{q})\right)\delta\left\{\omega-\omega(\mathbf{q})\right\} + n_j(\mathbf{q})\,\delta\left\{\omega+\omega(\mathbf{q})\right\}\right) \tag{3.30}$$

$$H^j_{\mathbf{q}}(\mathbf{Q}) = \sum_d \frac{f_d(\mathbf{Q})}{\sqrt{M}_d}\exp\left(-W_d(\mathbf{Q}) + i\mathbf{Q}\cdot\mathbf{d}\right)\left\{\mathbf{Q}\cdot\sigma^{\mathbf{j}}_{\mathbf{d}}(\mathbf{q})\right\} \tag{3.31}$$

The phonon intensities described by 3.30 can be quite complicated. In general, long-wavelength acoustic modes are strongest near strong Bragg reflections. In this case, $\sigma^j_d(\mathbf{q})/M_d$ is approximately independent of the atom and can be factored out of the sum. In simple materials a similar argument suggests that optical modes are strongest near weaker Bragg peaks.[32] Figure 3.5 shows two calculations of the dynamical structure factor we used to determine where to measure along (00L). First, the $\mathbf{Q}\cdot\sigma_{\mathbf{d}}{}^j(\mathbf{q})$ term filters out only those modes with atoms moving in the direction of $\mathbf{Q}$. In addition, the intensity of these modes varies dramatically with $\mathbf{Q}$. For example, the optical mode near 25 meV is much more intense around $\mathbf{Q}$=5.5 or 8.5 than $\mathbf{Q}$=6.5 or 7.5. These calculations helped us determine that measurements of the phonon dispersion from (0.0,0.0,8.1) to (0.0,0.0,8.5) would provide the greatest intensity for the modes we were most interested in.

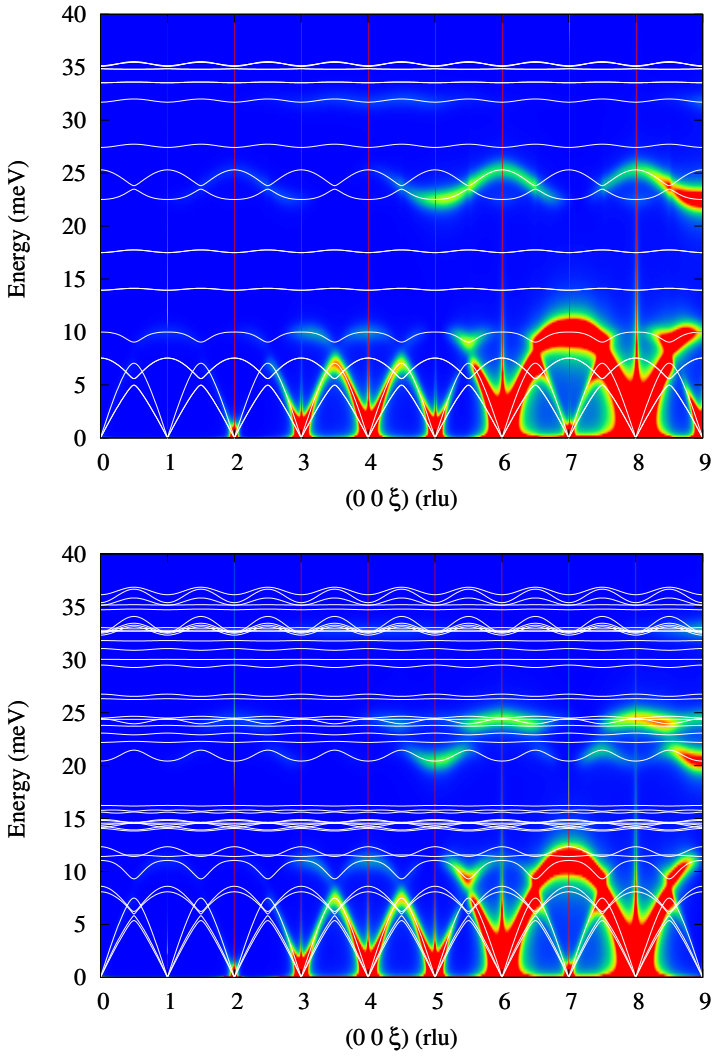

Figure 3.5 Images from LaFeAsO suggesting where to scan along (00L). The top figure is a nonmagnetic calculation, while the lower figure includes the antiferromagnetic order present below the lower-temperature orthorhombic phase. This study is discussed in chapter 6.

3.4.2 Resolution in Q

In addition to the energy resolution, fig. 3.6 shows how the size of the analyzer leads to a finite resolution in Q. Ignoring curvature, any spot on the analyzer can be described by an distance from the center, related to $\delta(2\theta)$ and ϕ, the later of which varies from 0 to 2π. At sectors 3 and 30 at the Advanced Photon Source at Argonne National Laboratory, the size of the analyzer is 10 cm and the distance from the sample to the analyzer are 6m and 9m, respectively.

For the case when the nominal Q is along the z-axis, one can write possible values of Q accepted by the analyzer as a function of θ, $\delta(2\theta)$ and ϕ. Since the energies associated with $\hbar\omega$ are 6 orders of magnitude larger than Q, one can assume $|K_i| = |K_f| = K$. Including this as well as conservation of momentum one can write possible values for Q as shown in Eqns 3.32.

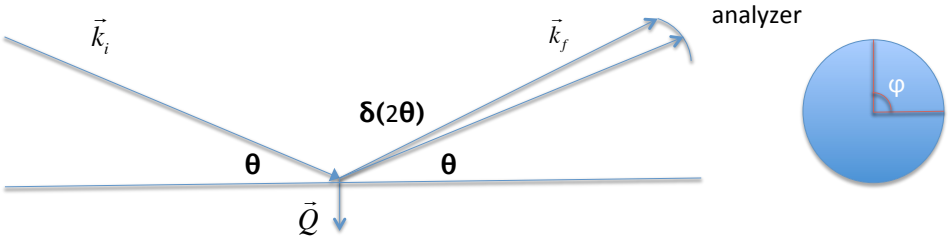

Figure 3.6 Finite resolution in **Q** can be described by the angles θ, $\delta(2\theta)$ and ϕ.

$$Q_x = K\left(\cos\theta\left(1-\cos\left(\delta 2\theta\cos\phi\right)\right)+\sin\theta\sin\left(\delta 2\theta\cos\phi\right)\right) \tag{3.32}$$

$$Q_y = -K\sin\left(\delta 2\theta\sin\phi\right) \tag{3.33}$$

$$Q_z = K\left(\sin\theta\left(1+\cos\left(\delta 2\theta\cos\phi\right)\right)+\cos\theta\sin\left(\delta 2\theta\cos\phi\right)\right) \tag{3.34}$$

We found sampling 5000 points sufficient for simulating constant-Q scans. Contour plots required less precision, and obtained good results with 1000 samples per point.

The effects of finite Q-resolution are strongest in modes whose energy is changing rapidly with Q, such as acoustic modes near the zone center. Figure 3.7 shows the calculated dynamical structure factor in LaFeAsO at (0.0,0.0,8.3) with both infinite Q-resolution and with the estimated Q-resolution at sector 30. The longitudinal mode near 5 meV is significantly broader, while the nearby optical mode is essential unchanged. In addition, the peak position is shifted to slightly lower energy. H. Fukui et al.[39] showed that for a phonon varying linearly with **q** the true energy center is at slightly higher energy than the centroid of the obtained signal. Consequently, corrections may be required to precisely determine the frequencies of acoustic modes at small-**q**.

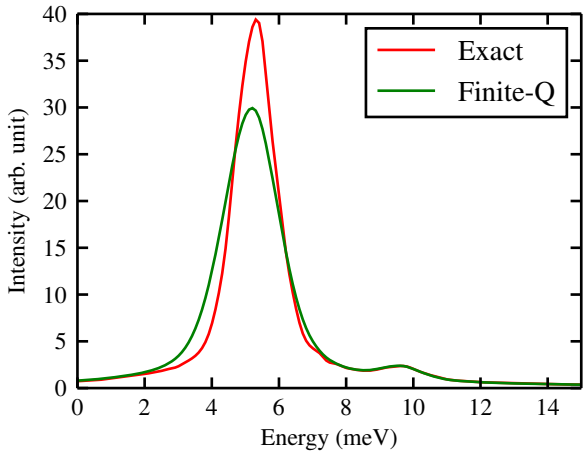

Figure 3.7 Comparison between the dynamic structure factor with infinite and finite Q-resolution at Q=(0.0,0.0,8.3) in LaFeAsO.

3.4.3 Debye-Waller factor and x-ray form factor

Both the x-ray form factor and the Debye-Waller factor decrease intensity of the phonon excitations with increasing Q. Including harmonic vibrations adds an additional term to the intensity of a Bragg peak called the Debye-Waller factor. Without any additional approximations, the Debye-Waller factor can be written as in Eqn. 3.35. It can be thought of as the mean-squared displacement of the atoms dotted with with Q^2. Therefore the intensity of the Bragg peaks decreases with increasing Q. This term is also present in the dynamical structure

factor, having the same effect.

$$W_d(\mathbf{Q}) = \frac{\hbar}{4M_d N} \sum_s \frac{|\mathbf{Q} \cdot \sigma_{ds}|}{\omega_s} \langle 2n_s + 1 \rangle \tag{3.35}$$

This expression can be greatly simplified by assuming assuming cubic symmetry and rewriting in terms of the phonon density of states, $Z(\omega)$. Assuming cubic symmetry, the average of $|Q \cdot \sigma|^2$ over a surface with given ω simplifies to $\frac{1}{3}Q^2$ This is a fair approximation in most non-cubic crystals[36]. The resulting expression is given in eqn. 3.36. For crystals containing different elements, the density of states is replaced by the partial density of states. The phonon density of states can be calculated from the real-space force constants using, for example, the QHA package in Quantum Espresso.

$$W(\mathbf{Q}) = \frac{\hbar Q^2}{4M} \int_0^\infty d\omega \frac{Z(\omega)}{\omega} \coth\left(\frac{1}{2}\hbar\omega\beta\right) \tag{3.36}$$

Considering the two-dimensional nature of the iron pnictides and the difficulty we had using the QHA package with the crystals structures of the iron pnictides, we chose a different approach for calculating the Debye-Waller factor. The sum over $\mathbf{q}$ can be rewritten as an integral over the brillouin zone and the Bose occupation written out explicitly. The volume integral can then be calculated using the tetrahedron method[40, 41]. A Monkhorst and Pack mesh can be created from the lattice vectors[42]. Each hexahedron is then broken into six tetrahedrons of equal volume. The integral over the entire Brillouin zone is simply the sum of the integral over each tetrahedron. To second order, the integral over the tetrahedron is simply the function evaluated at the center point multiplied by the volume. This approximation improves as the number of tetrahedrons increases. To avoid repeating the calculation for each value of $\mathbf{Q}$, the nine potential components of the phonon eigenvector were computed, and the dot product calculated later.

$$W_d(\mathbf{Q}) = \frac{\hbar}{4M_d \Omega_{BZ}} \int_{\Omega_{BZ}} \sum_s \frac{|\mathbf{Q} \cdot \sigma_{ds}|^2}{\omega_s} \coth\left(\frac{1}{2}\hbar\omega_s\beta\right) \tag{3.37}$$

We confirmed the validity of our calculation by comparing results in FCC aluminium calculated from both the phonon density of states and direct integration. Fig. 3.8 shows the

dynamical structure factor of LaFeAsO at Q=(0.0,0.0,8.3) with an without the Debye-Waller factor and how it decreases intensity of the phonon excitations with increasing **Q**.

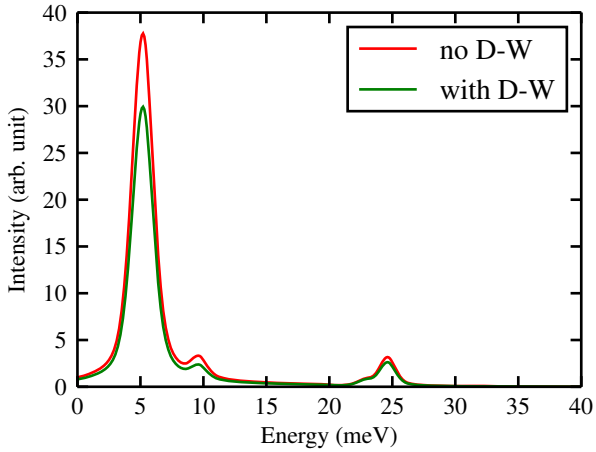

Figure 3.8 Comparison between the dynamical structure factor with and without the Debye-Waller factor at Q=(0.0,0.0,8.3) in LaFeAsO

The x-ray form factor also decreases intensity of the phonon excitations with increasing **Q**. The preferred approach for computer applications are numerical approximations to the x-ray form factor. The x-ray form factor has been parameterized by Waazmaier and Kirfel as the sum of five Gaussians plus a constant term[1]. Values of a_i and b_i used for LaFeAsO from ref [1] are given in Tbls. 3.4.3 and 3.4.3. This parameterization is valid over the range of $Q = sin(\theta)/\lambda$ from 0 to 6Å^{-1}, which is similar to the largest values of **Q** used in these investigations.

$$f_{el}(Q) = \sum_{i=1}^{5} a_i \exp\left(-b_i Q^2\right) + c \tag{3.38}$$

Table 3.1 Fitted values of a_i for the x-ray form factor from ref.[1]

Atom	a_1	a_2	a_3	a_4	a_5
La	19.966018	27.329654	11.018425	3.086696	17.335454
Fe	12.311098	1.876623	3.066177	2.070451	6.975185
As	17.025643	4.503441	3.715904	3.937200	6.790175
O	2.960427	2.08818	0.637853	0.722838	1.142756

Fig. 3.9 shows the fitted form factor for La,Fe,As and O from 0 to 6Å. at $Q = 0$ the x-ray form factor is equal to the atomic number of each element. The x-ray form factor decreases

Table 3.2 Fitted values of b_i and c for the x-ray form factor from ref.[1]

Atom	b_1	b_2	b_3	b_4	b_5	c
La	3.197408	0.003446	19.955492	141.381979	0.341817	-21.745489
Fe	5.009415	0.014461	18.743041	82.767874	0.346504	-0.304931
As	2.597739	0.003012	14.272119	50.437997	0.193015	-2.984117
O	14.182259	5.936858	0.112726	34.958481	0.390240	0.027014

rapidly with increasing Q, reducing the intensity at zones far out in reciprocal space. In addition, relative changes between the different atoms changes the intensity of different modes at a single value of Q.

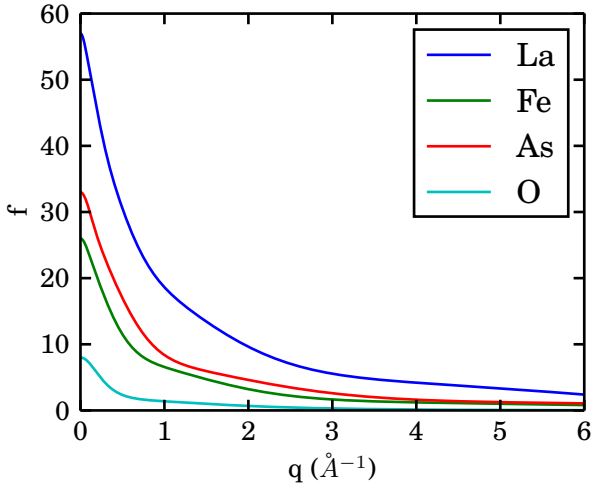

Figure 3.9 Plot of the fitted x-ray form factor from 0 to 6Å. Fitting parameters are from ref.[1] and listed in Tbls. 3.4.3 and 3.4.3.

Fig. 3.10 recreates the plots used during measurements of LaFeAsO covered in chapter 5. Including finite Q-resolution, the Debye-Waller factor, and the x-ray form factor leads to qualitative and quantitative changes in the calculated dynamical structure factor. In particular the relative intensity of the optical mode near 25 meV is much stronger near Q=(005) than Q=(008). Compared to the region suggested by our earlier calculations and measured in chapter 5, measurements at smaller Q might have provided better intensity.

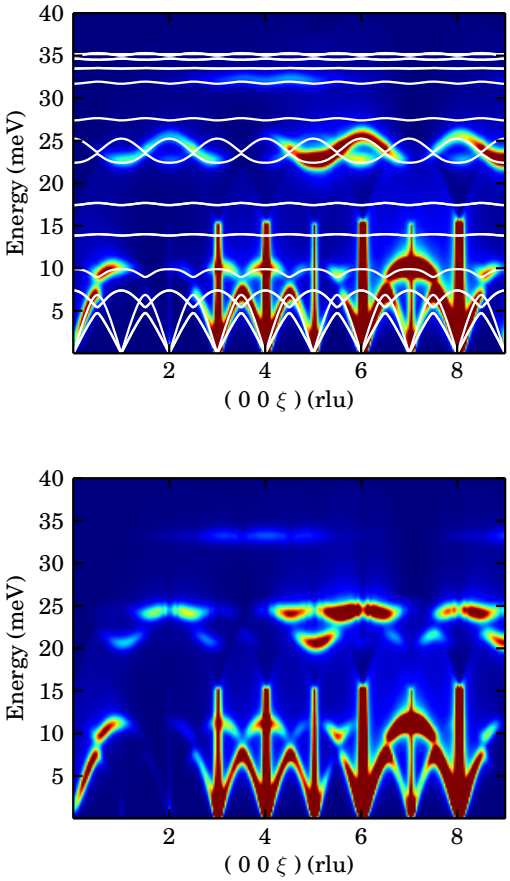

Figure 3.10 Images from LaFeAsO suggesting where to scan along (00L). The top figure is a nonmagnetic calculation and the lower figure includes the SDW antiferromagnetic order of the lower-temperature orthorhombic phase. The inclusion of the Debye-Waller factor, x-ray form factor, the effects of finite-Q resolution leads to qualitative and quantitative changes in the dynamical structure factor.

CHAPTER 4. Motivation

The discovery of iron-based superconductors in 2008 created a very exciting time to be studying physics. New and exciting work was being done on an extremely rapid timeline with new preprints released on the arXiv every night, leading to a large number of publications and many sessions at the following APS March Meetings. Previously I had spent some time learning how to perform electronic structure calculations using density functional theory and phonon calculations in vanadium oxide. Consequently, I was very fortunate to have access to exciting new materials with many interesting questions as well as some knowledge of a method to study them. In this section we motivate the studies we undertook and discuss some of the work coming out at the same time.

4.1 Importance of phonons on materials properties

Electronic structure calculations often begin with a static lattice model where one places the atomic nuclei at fixed positions in the unit cell. The Born-Oppenheimer approximation discussed in chapter 2 allows one to decouple the electronic and ionic motion and there are many examples of physical properties where the phonon contribution is comparable to or larger than the electronic contribution. Neglecting atomic motion leads to failures in explaining some equilibrium properties, transport properties, and interactions with radiation.

For an example of the importance of lattice vibrations, consider the specific heat. The electronic contribution to the specific heat in metals is linear, which is observed in metals at low temperatures. Measurements however show a more complicated T^3 dependence at higher temperatures. This same T^3 dependence is observed in insulators at low temperatures. Lattice vibrations explain this behavior and in fact become the dominant contribution in the high-

temperature limit.

Lattice parameters depend on temperature and calculation of this thermal expansion requires the electronic and phonon contribution to the free energy. Even in metals, the electronic contribution is only comparable below 10K. The entropy introduced by phonon excitations is important for understanding phase transitions with temperature. Similarly melting, where the ions leave their equilibrium position, also requires knowledge of the size of the atomic motion with temperature.

In the BCS theory of superconductivity, named after it's authors Bardeen, Cooper, and Schrieffer, the development of Cooper pairs comes from coupling of electrons via the crystal lattice. Consequently, phonons and in particular the electron-phonon coupling are interesting quantities and are the first mediator to be considered and studied in a newly discovered superconductor.

Inelastic X-ray and neutron scattering on crystals elucidate phonons and both methods are often exploited to measure the phonon dispersion in materials. Scattered x-rays and neutrons lose energy in discrete amounts dependent on the change of momentum. Thermal vibrations of the ions are responsible for the Debye-Waller factor that diminishes the Bragg peaks.

4.2 Importance of phonons in the iron-based superconductors

The rush to the iron-based superconductors started with the discovery of superconductivity in F-doped LaFeAsO with a relatively high T_c of 26K[2]. Similar materials were soon discovered with $T_c{}'$s up to 55K[43]. These temperatures are very high for a conventional BCS superconductor. First principles calculations using density functional theory for LaFeAsO strongly suggest that electron-phonon coupling is not sufficient to explain superconductivity[44]. In addition, the crystal structures are two-dimensional, containing layers of iron and arsenic that somewhat resemble the copper and oxygen planes in the cuprate superconductors. The phase diagram with doping also resembles the cuprates. At low temperatures the parent compound is orthorhombic with striped antiferromagnetic order. Increasing temperature, the material goes through a magnetic and then a structural phase transition to a paramagnetic tetragonal phase. Doping the oxygen site with fluorine also leads to a structural and magnetic transition to a

paramagnetic tetragonal phase. At sufficiently low temperatures, however a superconducting region exists in close proximity to the structural and magnetic transition. While this field continues to evolve rapidly, Ref. [3] provides a thorough and general review of these materials through 2010. Below we give a few highlights to motivate the following chapters.

Superconductivity has many important applications. Their ability to carry current with minimal resistance make them potentially useful for power transmission. Superconducting wires are used in the most powerful electromagnets. They can conduct more current than copper wire and can maintain their field for very long periods of time. Cooling materials down to the temperatures where BCS materials superconduct requires much energy and expensive liquid helium. A higher superconducting temperature would reduce the cost and complexity of the cooling system and allow for much wider usage.

Given the scientific interest and potential applications of high temperature superconductivity, there have been many ensuing efforts to understand the possible electronic, magnetic and phononic mechanisms responsible for these properties. Such investigations have revealed intriguing information about the new Fe-As based materials. These systems display significant sensitivity to the lattice geometry. For example, DFT calculations show the size of the Fe moment is sensitive to the lattice parameters and As position. One thus expects strong magneto-structural coupling in these compounds[45].

A second family of materials was soon discovered with similar properties and a slightly different crystal structure. The Fe-As planes are present, but instead of being separated by a rare earth and oxygen, they are separated by only an alkaline earth metal. The material we focused on was $CaFe_2As_2$. Superconductivity is observed with doping on the Ca and Fe sites, though not with hydrostatic pressure. Experiments and calculations of the crystal structure and magnetism of $CaFe_2As_2$ under pressure show the dramatic sensitivity of the magnetic moment to changes in the atomic positions. One key example of this coupling in $CaFe_2As_2$ comes from the observation of a transition from the antiferromagnetic state to a non-magnetic "collapsed tetragonal" state under applied pressure.[46] In this case, a reduction of the c-axis lattice parameter by 9.5% is associated with the complete collapse of the Fe magnetic moment.[47] Superconductivity is observed with doping, but not with applied pressure.

The spin-polarized calculations in later chapters were motivated by strong antiferromagnetic correlations have observed by neutron scattering above the AFM ordering temperature (172K) in $CaFe_2As_2$[48] that extend up to and beyond room temperature[49]. Spin fluctuations have also been observed in powder samples of LaFeAsO[50, 51]. The iron moment becomes important for understanding magnetoelastic properties of these materials.

4.3 Phonon Measurements

Until recently[52], phonon measurements in 1111 materials were limited to the phonon density of states in polycrystaline samples. It might be expected that the presence of RO layers, which results in a larger spacing of the FeAs layers along the c-axis, might mitigate magnetic effects to some degree. Distinct features in the phonon DOS, likely associated with atomic displacements in the Fe-As plane, were observed at significantly lower energies than non-magnetic calculations suggest. It was noted (empirically) that softening of the Fe-As force constants by 30% brings the calculated phonon DOS into better agreement with the data.[53] T. Yildirim showed that including magnetism from the low-temperature tetragonal phase improves agreement between theory and experiment[45]. In addition, he notes that the modes remain quite harmonic and that the change in frequencies is likely due to a complicated renormalization of the force constants with magnetism and these changes were not limited to only Fe-As force constants.

Availability of single crystals has mostly limited measurements of the phonon dispersion to the 122 materials. The lattice vibrational frequencies associated with c-axis vibrations of alkali earth and As atoms in $CaFe_2As_2$ and $BaFe_2As_2$ [54, 55] have been shown by inelastic neutron and x-ray scattering to disagree with predictions of non-spin polarized DFT calculations. In particular, the energy splitting between c-axis phonon branches containing As displacements was found to be in strong disagreement with non-spin polarized calculations with theoretically determined lattice parameters. DFT calculations using the experimental lattice parameters and internal As position were in better agreement with the experimental data. Spin-polarized calculations with the striped antiferromagnetic order predict the internal As-parameter closer to experiment, giving some suggestions magnetism is important for calculating and understanding

phonons in these materials.

Similar discrepancies are present in the phonon density of states of $BaFe_2As_2$. T. Yildirim showed that including magnetism from the low-temperature tetragonal phase drastically improved agreement between theory and experiment. Other theoretical studies have shown that strong coupling between Fe magnetism and the As position leads to the softening of the Fe-As force constants, thereby explaining the observed phonon spectra.[56] Theoretical studies have shown that strong coupling between Fe magnetism and the As position leads to the softening of the Fe-As force constants, thereby explaining the observed phonon spectra.[56]

The goal of the following measurements and calculations were to determine the phonon dispersion in these materials to better understand its properties. In $CaFe_2As_2$ we were among the first groups to measure the phonon dispersion. Calculations were used to determine the effects magnetism had on phonons in the different phases. In LaFeAsO, we investigated the effect magnetism has on individual modes instead of the entire phonon DOS. In addition we calculated the phonon dispersion for different magnetic ordering to understand if features in the phonon dispersion were dependent on merely the moment on the iron or if the specific ordering had an effect.

CHAPTER 5. Influence of magnetism on phonons in $CaFe_2As_2$ as seen via inelastic x-ray scattering

A paper published in Physical Review B: Phys. Rev. B **79** 220511(R) (2009)

S. E. Hahn,[1] Y. Lee,[1] N. Ni,[1] A. Alatas,[2] B. M. Leu,[2] D. Y. Chung,[3] I. S. Todorov, [3] E. E. Alp,[2] M. G. Kanatzidis,[3,4] P. C. Canfield,[1] A. I. Goldman,[1] R. J. McQueeney,[1] and B. N. Harmon[1]

5.1 Abstract

In the iron pnictides, the strong sensitivity of the iron magnetic moment to the arsenic position suggests a significant relationship between phonons and magnetism. We measured the phonon dispersion of several branches in the high temperature tetragonal phase of $CaFe_2As_2$ using inelastic x-ray scattering on single-crystal samples. These measurements were compared to *ab initio* calculations of the phonons. Spin-polarized calculations imposing the antiferromagnetic order present in the low-temperature orthorhombic phase dramatically improve agreement between theory and experiment. This is discussed in terms of the strong antiferromagnetic correlations that are known to persist in the tetragonal phase.

5.2 Introduction

Iron-pnictide materials are currently the subject of enormous scientific activity. The discovery of superconductivity with T_c's up to 55K and the ensuing efforts to understand the

[1]Department of Physics and Astronomy and Ames Laboratory, Iowa State University, Ames, IA, 50011, USA
[3]Advanced Photon Source, Argonne National Laboratory, Argonne, IL 60439, USA
[4]Materials Science Division, Argonne National Laboratory, Argonne, IL 60439, USA
[6]Department of Chemistry, Northwestern University, Evanston, IL 60208, USA

possible electronic, magnetic and phononic mechanisms responsible have already revealed intriguing information[2, 43]. For example, first principles calculations using density functional theory for LaFeAsO strongly suggest that electron-phonon coupling is not sufficient to explain superconductivity[44]. Other calculations demonstrate the strong dependence of the iron magnetic moment on the arsenic atomic position suggesting an interplay between certain phonons and magnetism[57, 58, 59]. Experiments and calculations of the crystal structure and magnetism of $CaFe_2As_2$ under pressure show the dramatic sensitivity of the magnetic moment to changes in the atomic positions[46]. The motivation for the present investigation was to study phonons in $CaFe_2As_2$ to ascertain any anomalies related to the structure and possible magnetic interactions.

We report measurements of the phonon dispersion in the paramagnetic high-temperature tetragonal phase of single-crystal $CaFe_2As_2$ using inelastic x-ray scattering. Several phonon branches consisting of c-axis polarized As modes are observed to have energies and intensities in poor agreement with non-spin-polarized (NSP) band-structure calculations of the phonon dispersion and structure factor. However, the imposition of antiferromagnetic (AFM) ordering in the tetragonal phase by spin-polarized (SP) calculations brings the dispersion into better agreement with the experimental data. Strong antiferromagnetic correlations have been observed by neutron scattering above the AFM ordering temperature [48] and extend above room temperature[60]. In addition, X. F. Wang et. al.[61] measured a substantial linear increase in the magnetic susceptibility of $BaFe_2As_2$ up to 700K. Such behavior may indicate spin fluctuations above the AFM ordering temperature[62]. Similar behavior has also been reported for $CaFe_2As_2$ up to at least 300K[63]. Resistivity measurements also suggest spin fluctuations and spin scattering above the AFM transition temperature[64]. Given the known sensitivity of the Fe magnetic moment to the As z-position in the crystal, measurements and calculations of the phonon structure factor indicate an important coupling between local magnetic order and interatomic force constants.

5.3 Samples and Experimental Details

Samples of $CaFe_2As_2$ were prepared by two different research groups. The $CaFe_2As_2$ sample used for measurements along (110) was prepared by the Kanatzidis Group using a stoichiometric elemental mixture in Sn metal flux. Handling of all elements was carried out in a N_2-filled glove box and 0.2 grams of Ca, Fe, and As and 4.0 grams of Sn metal were used. The mixture was loaded into an alumina tube plugged with ceramic wool and sealed in a silica tube under vacuum. The mixture was heated to 1050°C for 14 hours and kept there for 8 hours, followed by cooling to 600°C at a rate of 20 $^{\circ C}/_{\text{hour}}$. The molten Sn flux was then filtered with a centrifuge. The resulting square plate crystals of $CaFe_2As_2$ were identified by X-ray powder diffraction.

All other measurements were performed on samples that were prepared by the Canfield Group out of Sn flux[65, 66] using a conventional high-temperature solution growth technique. Small Ca chunks, Fe and As pieces, as well as Sn shots were loaded into an alumina crucible according to the ratio Ca:Fe:As:Sn=2.13:3.74:4.28:89.84. A second "catch" crucible containing quartz wool was placed on top of this "growth" crucible. Both crucibles were then sealed into a quartz tube under 1/3 atmosphere Ar gas. The sealed quartz tube was heated to 1150°C, dwelled for 4 h, and then cooled to 600°C for 50 h. Once the furnace reached 600°C, the liquid was decanted from the platelike crystals.

Inelastic x-ray scattering measurements were performed at Sector-3-ID-C of the Advanced Photon Source at Argonne National Laboratory. The incident energy was set to 21.66 keV with an energy resolution of 2.379 meV full-width-at-half-maximum. Measurements were performed on a single crystal of $CaFe_2As_2$ measuring approximately 2 x 2 mm with a thickness of 100μm. The sample was mounted in both the $(H0L)$ and (HHL) tetragonal planes in a closed-cycle Helium refrigerator and most measurements were performed at room temperature, although some scans were also performed at lower temperatures.

Phonons were measured using constant-Q energy scans along the tetragonal $(0, 0, 5 + \xi)$, $(1, 0, 3 + \xi)$, $(1 + \xi, 0, 3)$, and $(\xi, \xi, 4)$ directions at room temperature. The energy transfer scale for each scan was calibrated for monochromator and analyzer temperature drifts. The

scans were fit to several peaks using a pseudo-Voigt line profile. The normalized pseudo-Voigt function is given in eq.5.1, where $f_G(x;\Gamma)$ and $f_L(x;\Gamma)$ are normalized Gaussian and Lorentzian functions respectively. The mixing parameter $\eta = 0.393$, and resolution full-width-at-half-maximum (FWHM) $\Gamma = 2.379\ meV$ was determined from fits to the elastic scattering width of Plexiglas,

$$f_{pV} = (1-\eta)\, f_G(x;\Gamma) + \eta f_L(x;\Gamma)\,. \tag{5.1}$$

Figures 5.1(a) and 5.1(b) show line scans consisting of several phonon excitations at $Q = (0,0,5.75)$ and $Q = (1.5,0,3)$ respectively along with fits to the data. The peak positions for these and other scans were obtained from the fits and used to construct the dispersion of phonon branches along the different scan directions.

5.4 Phonon Calculations

In order to understand the features of the phonon dispersion, the experimental measurements were compared to *ab initio* calculations of the phonons. The phonon dispersion was calculated using Density Functional Perturbation Theory (DFPT)[67]. There is not yet a consensus on the proper lattice parameters to use for these calculations. In nonmagnetic calculations, relaxing the lattice parameters results in a large contraction of the c-axis. In spin-polarized calculations, the lattice distorts into an orthorhombic structure. With these difficulties in mind, experimental lattice parameters were used[46]. In addition, there is controversy over the appropriate internal Arsenic parameter to use. We chose relaxed positions so that all forces were zero. For non-magnetic and spin-polarized calculations, the relaxed As z-position is $z_{As} = 0.3575$ and $z_{As} = 0.3679$ respectively. Mittal et. al.[59] use the experimental value of $z_{As} = 0.372(1)$. The pseudopotentials chosen used the Perdew-Burke-Ernzerhof (PBE) exchange correlation functional[68, 24]. Settings of an 8x8x8 k-mesh and 24 eV and 400 eV energy cutoffs for the wavefunctions and charge density were chosen to ensure that the precision of the calculated phonon dispersion was better than 1.0 meV. Due to the paramagnetic state of $CaFe_2As_2$ at room temperature, non-magnetic calculations were first performed.

Phonon frequencies were calculated on a 2x2x2 q-mesh, and then interpolated along several symmetry directions. The resulting phonon frequencies and eigenvectors were used to calculate the dynamical structure factor along the selected scan directions. The dynamical structure factor, which is proportional to the x-ray scattering intensity, is given in eq.5.2[36]. The Debye-Waller, $W_d(\mathbf{Q})$ factor was set equal to zero, and the scattering length is proportional to Z_d, the atomic number of the corresponding atom, and $\sigma^j_{\mathbf{d}}(\mathbf{q})$ is the eigenvector corresponding to the normalized motion of atom d in the j$^{\text{th}}$ phonon branch.

$$S_j(\mathbf{q},\omega) = \frac{\left|H^j_{\mathbf{q}}(\mathbf{Q})\right|^2}{2\omega_j(\mathbf{q})}\left(1+n_j(\mathbf{q})\right)\delta\left\{\omega-\omega(\mathbf{q})\right\} \tag{5.2}$$

$$H^j_{\mathbf{q}}(\mathbf{Q}) = \sum_d \frac{Z_d}{\sqrt{M_d}}\exp\left(-W_d(\mathbf{Q})+i\mathbf{Q}\cdot\mathbf{d}\right)\left\{\mathbf{Q}\cdot\sigma^{\mathbf{j}}_{\mathbf{d}}(\mathbf{q})\right\} \tag{5.3}$$

5.5 Discussion

For comparison with experiment, the delta functions were broadened with a pseudo-Voigt function whose parameters were chosen to match the experimental resolution. Fig.5.1 shows the comparison of the calculated structure factor to the data for two scans. For the scans shown, the non-magnetic calculations show poor agreement with the phonons observed near $\sim$ 17 and 20 meV. Figs.5.2(a) and 5.3(a) show several observed phonons (white dots) along $(00L)$ and $(H03)$ compared to the non-magnetic calculated phonon dispersion weighted by the structure factors.

The agreement between calculations and the data dramatically improve when spin-polarized calculations were performed using a 4x4x4 k-mesh in a supercell using the observed antiferromagnetic structure of orthorhombic $CaFe_2As_2$. PBE overestimates the magnetic moment, with a value of 2.39 μ_B/Fe versus 0.80(5) μ_B/Fe observed experimentally.[69] Similar discrepancies between the calculated and observed magnetic moment were discussed in phonon studies of $BaFe_2As_2$[70]. Software limitations prevented constraining the magnetic moments while performing phonon calculations. Fig.5.1 shows that the spin-polarized calculations not only provide better agreement with the phonon energies, but even the phonon intensities (eigenvectors) show marked improvement. Along $(00L)$ in fig.5.2(b), the agreement of the middle two branches at

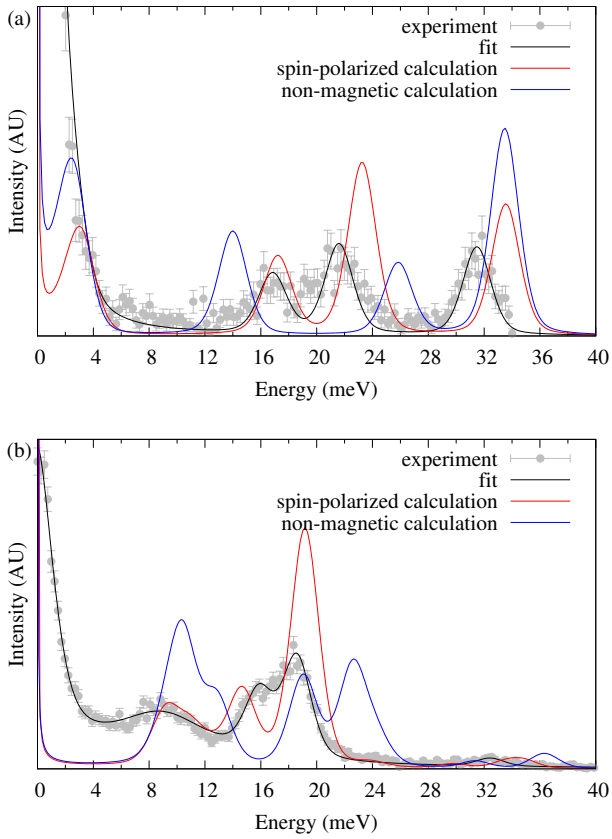

Figure 5.1 (a) Constant-Q line scan at $Q = (0, 0, 5.75)$. (b) Constant-Q line scan at $Q = (1.5, 0, 3.0)$. Experimental data are given by points and pseudo-Voigt fits by the solid line. Dashed red and blue lines correspond to calculations of the phonon structure factor for spin-polarized and non-magnetic calculations, respectively.

17 and 20 meV is dramatically improved by including the AF ordering which reduces the energy splitting of these two branches. Examination of the eigenvectors of these modes shows that they have Λ_1 symmetry and consist of longitudinally polarized Ca and As modes. SP calculations also show marked improvement for phonon branches in the same energy range along the (100) direction which connect to the two Λ_1 branches at the zone boundary. Fig.5.1(b) shows a scan at (1.5,0,3) where SP calculations dramatically improve agreement with the two Δ_3 phonon branches consisting of c-axis polarized transverse Ca and As modes in the 14-20 meV range. Fig.5.3(b) also shows improved agreement of the SP calculations of select phonon branches along (H03) to the measured dispersion. Measurements of other phonon branches along (110) and (10L) also show better agreement with the SP calculations (not shown).

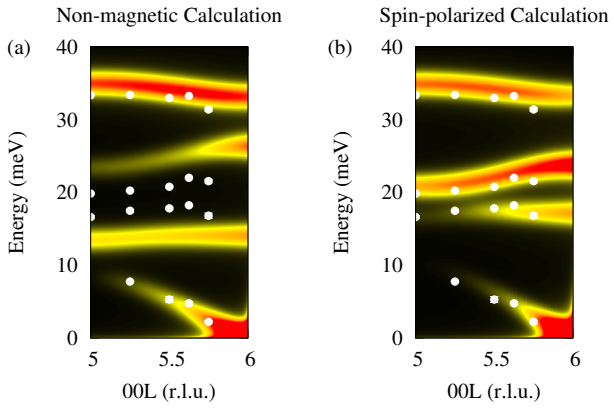

Figure 5.2 Phonon dispersion weighted by the structure factors along (00L) (a) without and (b) with antiferromagnetic order. The white dots are experimental data points.

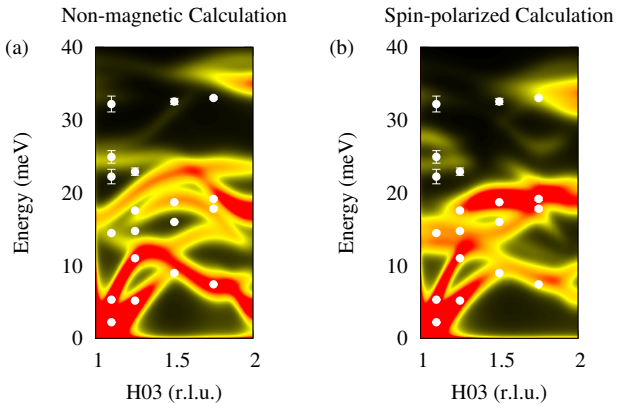

Figure 5.3 Phonon dispersion weighted by the structure factors along (H03) (a) without and (b) with antiferromagnetic order. The white dots are experimental data points.

Along both $(00L)$ and $(H00)$, the upper branch that softens with the introduction of AF order is associated with c-axis polarized As vibrations. Such modes have been predicted to have a strong influence on magnetism due to the sensitivity of the Fe moment on the As z-position.[58] Surprisingly, the lower branch starting at 17 meV are primarily c-axis polarized Ca modes in the NSP calculations. However, the spin-polarization introduces a strong mixing of these two branches of identical symmetry. Such mixing leads to the increased frequency and changes in intensity between SP and NSP calculations shown in figs.5.2 and 5.3.

The improved agreement of the spin-polarized calculations in the paramagnetic phase may seem surprising, however resistivity and magnetic susceptibility measurements suggest spin

fluctuations and spin scattering above the AFM transition temperature. Inelastic neutron scattering experiments indicate substantial antiferromagnetic correlations that persist above $T_N = 172K$[48] and up to at least 300 K.[60] These correlations are observed up to high energies ($>$ 60 meV) with correlation lengths up to 20Å, which indicates that strong AF correlations exist between sizable Fe moments even above T_N. Magnetism must be accounted for when considering the chemical binding and the interatomic forces. Cooling of the sample into the AF ordered orthorhombic phase at 140 K appears to have little influence on the position or linewidth of the phonons along $(00L)$.

5.6 Conclusions

In summary, we have measured the phonon dispersion along several high symmetry directions for the paramagnetic high temperature tetragonal phase of $CaFe_2As_2$. Spin-polarized first principles calculations are in better agreement with the experimental results than non-spin-polarized calculations. The effects of large theoretical magnetic moments and the details of the spin fluctuations at room temperature are issues still under investigation.

Recently, Mittal, et. al.[59]posted data from inelastic neutron scattering experiments and non-spin-polarized band structure calculations for $CaFe_2As_2$. This measurement is in excellent agreement with their published dispersion curves. Considerations of magnetic effects on the phonon force constants and density of states were posted by Mazin and Johannes[57] and Yildirim[58].

5.7 Acknowledgments

Work at the Ames Laboratory was supported by the U.S. Department of Energy, Basic Energy Sciences under Contract No. DE-AC02-07CH11358. Use of the Advanced Photon Source was supported by the U. S. Department of Energy, Office of Science, Office of Basic Energy Sciences, under Contract No. DE-AC02-06CH11357 and LDRD program at Argonne National Laboratory.

CHAPTER 6. Magnetism dependent phonon anomaly in LaFeAsO observed via inelastic x-ray scattering

A paper submitted to Physical Review B

S. E. Hahn,[1,2] G. S. Tucker,[1,2] J.-Q. Yan,[3,4] A. H. Said,[5] B. M. Leu,[5] R. W. McCallum,[6] E. E. Alp,[5] T. A. Lograsso,[2,6] R. J. McQueeney[1,2] and B. N. Harmon[1,2]

6.1 Abstract

The phonon dispersion was measured at room temperature along (00L) in the tetragonal phase of LaFeAsO using inelastic x-ray scattering. Spin-polarized first-principles calculations imposing various types of antiferromagnetic order are in better agreement with the experimental results than nonmagnetic calculations, although the measurements were made well above the magnetic ordering temperature, T_N. Splitting observed between two A_{1g} phonon modes at 22 and 26 meV is only observed in spin-polarized calculations. Magneto-structural effects similar to those observed in the AFe_2As_2 materials are confirmed present in LaFeAsO. The presence of Fe-spin is necessary to find reasonable agreement of the calculations with the measured spectrum well above T_N. On-site Fe and As force constants show significant softening compared to nonmagnetic calculations, however an investigation of the real-space force constants associates the magnetoelastic coupling with a complex renormalization instead of softening of a specific pairwise force.

[1]Department of Physics and Astronomy, Iowa State University, Ames, IA, 50011, USA
[2]Division of Materials Science and Engineering, Ames Laboratory US-DOE, Iowa State University, Ames, IA 50011, USA
[3]Materials Science and Technology Division, Oak Ridge National Laboratory, Oak Ridge, TN, 37831, USA
[4]Department of Materials and Engineering, The University of Tennessee, Knoxville, TN, 37996, USA
[5]Advanced Photon Source, Argonne National Laboratory, Argonne, IL 60439, USA
[6]Division of Materials Science and Engineering, Ames Laboratory US-DOE, Iowa State University, Ames, IA 50011, USA

6.2 Introduction

Despite rather convincing arguments that superconductivity in the AFe_2As_2 (A=Ca,Sr,Ba,Eu) and RFeAsO (R=La,Ce,Pr,Nd,Sm,Gd)-based compounds does not originate from conventional electron-phonon coupling,[44] these systems do display significant sensitivity to the lattice geometry. For example, the size of the Fe moment is sensitive to the lattice parameters and As position, as shown by Density functional theory (DFT) calculations. One thus expects strong magneto-structural coupling in these compounds.[45] Also, measurements of the room temperature phonon density-of-states (DOS) in LaFeAsO indicated some disagreement with non-spin-polarized DFT calculations.[71, 72] Distinct features in the phonon DOS, likely associated with atomic displacements in the Fe-As plane, were observed at significantly lower energies than non-magnetic calculations suggest. It was noted (empirically) that softening of the Fe-As force constants by 30% brings the calculated phonon DOS into better agreement with the data.[53] Theoretical studies have shown that strong coupling between Fe magnetism and the As position leads to the softening of the Fe-As force constants, thereby explaining the observed phonon spectra.[56]

While these magnetostructural effects are well documented in the AFe_2As_2-based systems, it is not clear if the same effects are present in the RFeAsO system. One key example of this coupling in $CaFe_2As_2$ comes from the observation of a transition from the antiferromagnetic state to a non-magnetic "collapsed tetragonal" state under applied pressure.[46] In this case, a reduction of the c-axis lattice parameter by 9.5% is associated with the complete collapse of the Fe magnetic moment.[47]

The lattice vibrational frequencies associated with c-axis vibrations of Ca and As atoms in $CaFe_2As_2$ and $BaFe_2As_2$ [73, 54, 55] have been shown by inelastic neutron and x-ray scattering to disagree with predictions of non-spin polarized DFT calculations. In particular, the energy splitting between c-axis phonon branches containing As displacements was found to be in strong disagreement with non-spin polarized calculations. Ultimately, spin-polarized calculations in the local spin density approximation that include the AFM order present at lower temperatures were required to bring the calculated phonon dispersion into better agreement with room

temperature measurements.[45] Our group was able to confirm the role of magnetism in c-axis polarized Ca and As modes in $CaFe_2As_2$ using single-crystal inelastic x-ray scattering (IXS) measurements at the Advanced Photon Source (APS) in combination with spin-polarized calculations using the Perdew-Burke-Ernzerhof (PBE) exchange-correlation functional.[73]

It might be expected that the presence of RO layers, which results in a larger spacing of the FeAs layers along the c-axis, might mitigate these effects to some degree. However, the difficulty of synthesizing RFeAsO in single-crystalline form has prevented a quantitative confirmation of similar magneto-structural coupling across the AFe_2As_2 and RFeAsO systems. Recently single crystal samples of LaFeAsO have become available. [52] IXS phonon data was recently reported on $PrFeAsO_{0.9}$ [53] and SmFeAsO[74] single-crystals, however the dispersions were only measured along the (100) direction. Also, the role of spin-phonon coupling could not be ascertained since results were compared only to non-spin-polarized LDA calculations.

6.3 Sample and Experimental Details

LaFeAsO single crystals were synthesized in an NaAs flux at ambient pressure as described elsewhere.[52] Inelastic x-ray scattering measurements were performed on the HERIX instrument at sector 30-ID-C of the Advanced Photon Source at Argonne National Laboratory with incident beam energy of 23.724 keV and with an energy resolution of 1.44 meV.[33, 34] Scattering is described in terms of the tetragonal P4/nmm unit cell where $\mathbf{Q} = \frac{2\pi}{a}(h\mathbf{i} + k\mathbf{j}) + \frac{2\pi}{c}l\mathbf{k}$. The vectors $\mathbf{i}$, $\mathbf{j}$, and $\mathbf{k}$ are the fundamental translation unit vectors in real space. Below T_S=156K, the sample transforms to an orthorhombic structure with space group Cmma. [75, 76] The relationship between the Miller indices in the tetragonal P4/nmm and orthorhombic Cmma phase are, $h = (H_o + K_o), k = (H_o - K_o)$, and $l = L_o$. Below the magnetic ordering temperature T_N=138K, the sample develops long-range spin-density wave (SDW) AFM order. The sample was mounted in the (hhl) plane in a displex for low temperature studies, and the displex was attached to a 4-circle diffractometer.

Based on previous studies of c-axis polarized phonons in $CaFe_2As_2$, we focused our study on phonon branches along the $(0, 0, 8+\xi)$ direction in the Brillouin zone. In order to study the dispersion and potential line broadening of the phonon modes, the scans were fit to several peaks

using a pseudo-Voigt line profile. The normalized pseudo-Voigt function is given in Eqn. 6.1, where $f_G(x;\Gamma)$ and $f_L(x;\Gamma)$ are normalized Gaussian and Lorentzian functions respectively. The mixing parameter $\eta = 0.74$, and resolution full-width-at-half-maximum (FWHM) $\Gamma = 1.44$ meV was determined from fits to the elastic scattering width of Plexiglas.

$$f_{pV} = (1-\eta)\, f_G(x;\Gamma) + \eta f_L(x;\Gamma) \tag{6.1}$$

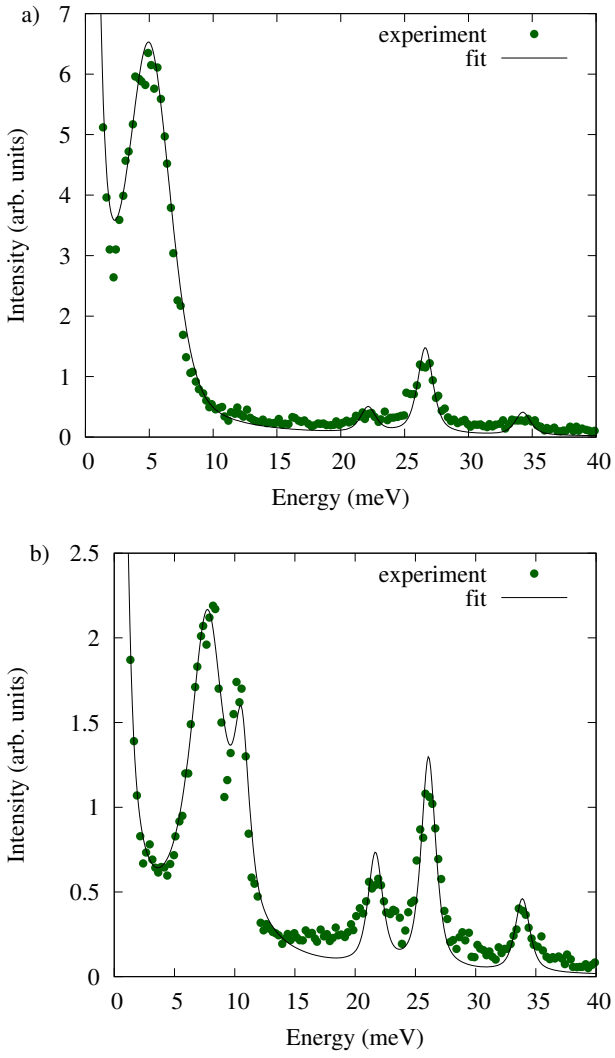

Figure 6.1 (color online) Energy scan at constant-Q at a) $Q = (0.0, 0, 8.3)$ and b) $Q = (0.0, 0, 8.5)$ measured at room temperature on LaFeAsO. Experimental data are given by solid green points. The black line is fit using a pseudo-Voigt function.

Figure 6.1 shows a line scan consisting of several phonon excitations at $\mathbf{Q} = (0, 0, 8.3)$

and $\mathbf{Q} = (0, 0, 8.5)$ at room temperature. The peak positions for these and other scans were obtained from fits and used to construct the dispersion of phonon branches along the different scan directions, as shown in Fig. 6.2. The intensity of the phonon modes is also represented in Fig. 6.2 by the diameter of the circles.

Table 6.1 Theoretically relaxed and experimentally observed z-position for La and As atoms, and the associated magnetic moment per Fe atom and total energy. In each case the experimental lattice parameters of ($a = 4.03533$Å, $c = 8.74090$Å) were used.[2, 3]

	NM	SDW	Striped	Checkerboard	Exp.[2, 3]
z_{La}	0.13993	0.13875	0.13883	0.13887	0.14154
z_{As}	0.63829	0.64820	0.64770	0.64401	0.6512
μ_{Fe}	0.0	2.32	2.30	1.91	0.36-0.78
E(Ry)	0.0	-0.032	-0.033	-0.009	

6.4 Phonon Calculations

In order to understand the features of the phonon dispersion, the experimental measurements were compared to *ab initio* calculations of the phonons. The phonon dispersion was calculated using DFT and Density Functional Perturbation Theory (DFPT).[77] There are significant differences in the experimental lattice parameters and parameters from the "relaxed" structure with the lowest calculated energy. Also, in spin-polarized calculations with the experimentally observed AFM order, the lattice distorts into the orthorhombic Cmma structure observed experimentally at lower temperatures. With these difficulties in mind, the experimental lattice parameters at room temperature in the tetragonal phase ($a = 4.03533$Å , $c = 8.74090$Å) were used for all calculations.[2, 3] In addition, there is debate over the appropriate internal z-parameter to use for the position of lanthanum and arsenic atoms.[78, 73, 79, 45] For better accuracy of the calculated phonons, we chose the calculated relaxed positions where all forces were zero. Structural parameters used for the non-magnetic and spin-polarized calculations as well as experimental measurements are given in table 6.1. The pseudopotentials chosen used the Perdew-Burke-Ernzerhof (PBE) exchange correlation functional.[80, 24] Settings of an 8x8x4 (nonmagnetic), 4x4x4 (striped & SDW) and 8x8x2 (checkerboard) k-mesh and 50 Ry and 660 Ry energy cutoffs for the wavefunctions and charge density were chosen to ensure meV precision

of the calculated phonon dispersion. These parameters are similar to other phonon calculations of LaFeAsO.[81, 44] Phonon frequencies were calculated on either a 4x4x2 (nonmagnetic), 2x2x2 (striped & SDW) or 4x4x1 (striped) q-mesh and then interpolated along several symmetry directions. The resulting phonon frequencies and eigenvectors were used to calculate the dynamical structure factor along the selected scan directions. The dynamical structure factor, which is proportional to the x-ray scattering intensity, is given in Eqn. 6.2.[36, 32, 35] In these equations, $W_d(\mathbf{Q})$ is the Debye-Waller factor, $n_j(\mathbf{q})$ is the Bose-Einstein distribution, $f_d(\mathbf{Q})$ is the x-ray form factor, and $\sigma^j_{\mathbf{d}}(\mathbf{q})$ is the eigenvector corresponding to the normalized motion of atom d in the j$^{\text{th}}$ phonon branch. While the DFT calculation does not include temperature dependence, the Bose-Einstein distribution was set to 300K.

$$S_j(\mathbf{q},\omega) = \frac{\left|H^j_{\mathbf{q}}(\mathbf{Q})\right|^2}{2\omega_j(\mathbf{q})}\left(1+n_j(\mathbf{q})\right)\delta\left\{\omega-\omega_j(\mathbf{q})\right\} \tag{6.2a}$$

$$H^j_{\mathbf{q}}(\mathbf{Q}) = \sum_d \frac{f_d(\mathbf{Q})}{\sqrt{M_d}}\exp\left(-W_d(\mathbf{Q})+i\mathbf{Q}\cdot\mathbf{d}\right)\left\{\mathbf{Q}\cdot\sigma^{\mathbf{j}}_{\mathbf{d}}(\mathbf{q})\right\} \tag{6.2b}$$

$$W_d(\mathbf{Q}) = \frac{\hbar}{4M_d\Omega_{BZ}}\int_{\Omega_{BZ}}\sum_j \frac{|\mathbf{Q}\cdot\sigma_{dj}|}{\omega_j}\left\langle 2n_j(\mathbf{q})+1\right\rangle \tag{6.2c}$$

Both the x-ray form factor and the Debye-Waller factor decrease intensity of the phonon excitations with increasing Q. The preferred approach for computer applications are numerical approximations to the x-ray form factor. The x-ray form factor has been parameterized by Waazmaier and Kirfel as the sum of five Gaussians plus a constant term.[1] The Debye-Waller factor, calculated using Eqn. 6.2c, can be thought of as the mean-squared value of the displacement each atom dotted with $\mathbf{Q}$. The volume integral was calculated using the tetrahedron method [40, 41] on a 16x16x8 (nonmagnetic), 16x16x4 (checkerboard) and 12x12x12 (SDW & striped) Monkhorst-Pack q-point grid.[42] To second order, the integral over the tetrahedron is simply the function evaluated at the center point multiplied by the volume. To avoid repeating the calculation for each value of Q, the nine potential components of the phonon eigenvector were stored and the dot product calculated later.

The delta function in ω was convoluted with the elastic scattering width of Plexiglas measured on analyzer 5. The pseudo-Voigt function fits well to the center of each peak, but small

discrepancies exist in the tail. To minimize this effect a discrete linear convolution between the raw experimental data and simulated delta functions (single point on a grid) was performed numerically.

In addition to the energy resolution, the diameter of the analyzer leads to a finite resolution in **Q**. Slightly different positions on the analyzer can be described by a radial component, determined from the size of the analyzer (10 cm) and the distance from the sample to the analyzer (9 m), and an angular component covering the entire circle. Values of **Q** accepted by the analyzer can be written as a function of these two variables. 5000 samples from a pseudo-random number generator gave sufficient precision for convolution of constant-**Q** scans with the **Q**-space resolution. Due to the lower required precision 1000 samples were used for each contour plot.

6.5 Discussion

Figure 6.1 shows a constant-**Q** energy scan at $(0, 0, 8.3)$ and $(0, 0, 8.5)$ at room temperature. Experimental data are given by the green points and pseudo-Voigt fits by the solid black line. The default values for η and Γ only account for the energy resolution. At (0,0,8.3) the fit on the acoustic mode at 5 meV, however, is adjusted by including η and Γ as variables. The fitted values of η and Γ are 0.48 ± 0.07 and 3.96 ± 0.09, respectively. Optical modes are present at 22, 27, and 34 meV. At (0,0,8.5) the fit on the acoustic mode at 8 meV, however, was adjusted by setting $\eta = 1.0$ (Lorentzian function) and including Γ as a variable. The fitted value of Γ is 3.67 ± 0.12 meV. A nearby optical mode is present at 11 meV, along with three other modes at 22, 26 and 34 meV, respectively.

Fig. 6.3 shows several calculations of the dynamical structure factor at **Q**=$(0, 0, 8.5)$ which can be directly compared to Fig. 6.1b. The red dotted line is a non-magnetic calculation. Frequencies for the acoustic and lowest optical modes are reasonable, but the calculated intensity of the optical mode is too high. Attempts to include the experimental uncertainty in **Q** could not reproduce the observed broadening of the acoustic mode, meaning it is not an artifact of Q-space resolution. The phonon excitation near 24 meV consists of two modes separated by 0.2 meV. At the zone boundary, lower and upper A_{1g} modes consist of As and La motion, respec-

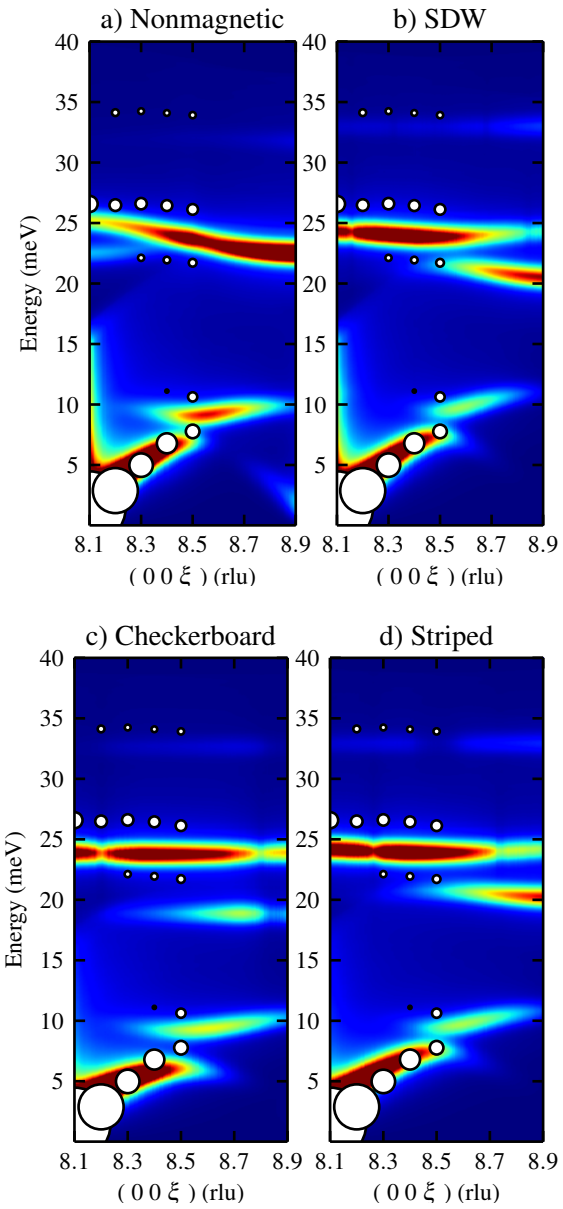

Figure 6.2 (color online) Contour plots of the calculated dynamical structure factor along (00L). Values range from blue (no intensity) to red (high intensity), and have been multiplied by the energy to improve visibility of the optical modes. The white dots show the experimentally determined frequencies, as described in the text, with the intensity shown by the size of the dot. a) Nonmagnetic calculation b) SP calculation with SDW ordering, c) SP calculation with checkerboard ordering. d) SP calculation with striped ordering.

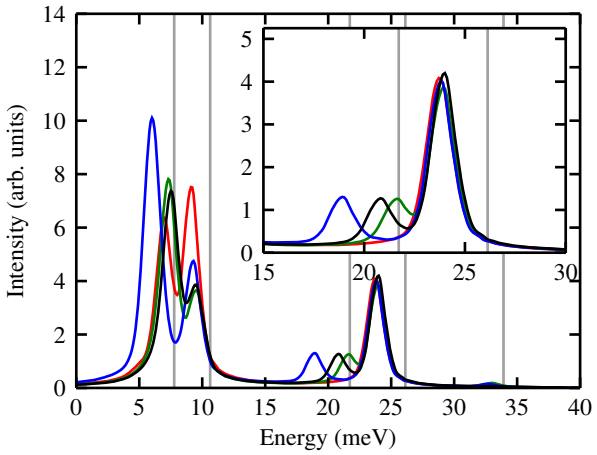

Figure 6.3 (color online) Dynamical structure factor calculation of constant-Q line scan at $Q = (0, 0, 8.5)$. The dotted red line corresponds to non-magnetic calculations of the dynamical structure factor. The solid green line corresponds to spin-polarized calculations imposing the SDW AFM ordering observed at lower temperatures. The black dashed line and blue dashed-dotted lines correspond to spin-polarized calculations with a striped (ferromagnetic along c) and checkerboard ordering, respectively. The experimentally observed frequencies in Fig. 6.1b are shown with vertical grey lines.

tively, polarized along the c-axis. At the zone center, these modes are mixed, each containing both La and As motion and the upper mode contributes 80% of the structure factor. This result from the nonmagnetic calculation is inconsistent with the measurements, where these two modes are clearly split by 4 meV at (0,0,8.5). While the calculated frequencies agree with other published phonon dispersions,[81, 44] they are a few meV lower in energy than observed. Small changes in lattice parameters are not responsible, as an unphysical 7% reduction in the unit cell volume is required to stiffen this phonon mode in the nonmagnetic calculation to the observed value. While this discrepancy exposes limits on the accuracy of these DFT calculations, this should not detract from qualitative changes between calculations, such as the splitting of the A_{1g} branches, that are also observed experimentally. At both values of Q, the 32 meV feature consists of both Fe and As motion, but the intensity is extremely weak.

In the spin-polarized calculation corresponding to the observed stripe AFM structure (Fig. 6.4b), the effect of the magnetization on Fe is to strongly split these two branches at (0,0,8.5)

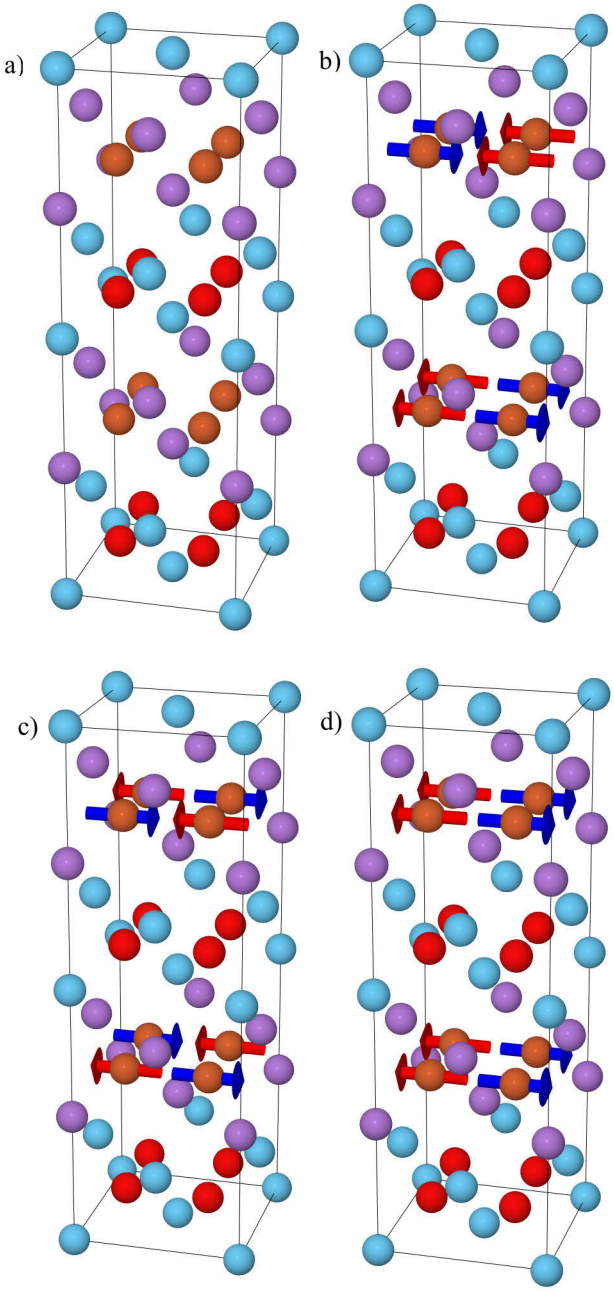

Figure 6.4 (color online) Different AFM order used in the calculations. La atoms are light blue, O atoms green, As atoms purple and Fe atoms brown. The red and blue arrows show up and down spin, respectively. a) expanded non-magnetic unit cell, b) experimentally observed SDW, c) Checkerboard ordering d) striped ordering aligned ferromagnetically along the *c*-axis

with the 21 meV excitation, containing As motion, lowering in energy by approximately 8.6%. The ratio of intensities between the acoustic and nearby optical mode moves in the direction of, though slightly more than, what is observed experimentally. The 24 meV peak is primarily La motion. The intensity of the 32meV feature is 5.2 times stronger, in better agreement with experiment.

In order to better understand the importance of the specific magnetic order and size of the Fe moment on the lattice dynamics, two additional calculations were performed in hypothetical magnetic structures. First is the "checkerboard" magnetic structure, shown in Fig. 6.4c. It is a tetragonal space group, where Fe neighbors have opposite spins. This calculation converges to a solution 0.023 Ry higher in energy and energy and with an 18% smaller magnetic moment per Fe atom. The acoustic mode is slightly softer and has greater intensity. The 21 meV excitation, containing As motion, is lower in energy by approximately 19.9%. The intensity of the 32meV feature is 2.9 times stronger than in the nonmagnetic calculation.

Second is the CeFeAsO structure,[82] also referred to as "striped," and shown in Fig. 6.4d. It is an orthorhombic space group with ferromagnetic coupling of Fe moments along the c-axis. The dynamical structure factor for this material is shown with black dashes in Fig. 6.3. The frequency and intensity of the acoustic and optical modes at 8 and 11 meV are nearly identical. Once again, the effect of the magnetization on Fe is to strongly split these branches, with the 21 meV excitation lowering in energy by approximately 11.9%. The intensity of the 32meV feature is half as strong as the nonmagnetic calculation.

Fig. 6.2 compiles all of the experimental data and calculations of the different magnetic structures by showing several contour plots of the dynamical structure factor along $(00L)$. Values of calculated intensities range from blue (low intensity) to red (high intensity), and have been multiplied by the energy to improve visibility of the optical modes. The white dots show the experimentally determined frequencies with the intensity shown by the size of the dot. In each case, calculations with a magnetic moment on the Fe show splitting between the two A_{1g} modes near 24 meV. At the zone center, the upper mode softens by 3.7 (SDW) - 5.3 (checkerboard) % and the lower mode softens by 9.1 (SDW) - 16.6 (checkerboard) %. Calculated frequencies of these two modes are a few meV lower than observed. Comparing

nonmagnetic and spin-polarized calculations, the frequency of the zone boundary the upper La-As mode is essentially unchanged ($< 0.6\%$). The intensity of the lower mode is strongest near (0,0,9), and the intensity of the upper mode is strongest near (0,0,8). The frequency of the lower mode differs by 2 meV. The SDW calculation best matches the experimental frequency, but the checkerboard pattern best matches the observed splitting between these two modes. We note that the checkerboard ordering also introduces a pronounced softening of the longitudinal acoustic mode when compared to the non-magnetic calculation and other magnetically ordered structures. Finally, we point out that the intensity of the optical mode near 10 meV is highest in nonmagnetic calculation. Overall changes in the phonon frequencies and intensities indicate the complex and subtle effects that magnetic ordering has on the lattice dynamics.

Despite the changes introduced by magnetic order, all the spectra are qualitatively similar for different magnetic orders, and in better agreement with experiment compared with non-magnetic calculations. This might be understood to occur as a consequence of Fe moments still being present above T_N, though without long-range order.[49] Compared to nonmagnetic calculations, imposing an AFM ordering better describes phonons in LaFeAsO. Consequently, it is likely that the presence of Fe moments, ordered or not, affects the force constants. Considering only z-polarized phonon branches containing La and As motion significantly reduces the number of force constants that contribute. First, only the "zz" term in the 3x3 force constant tensor can contribute, greatly simplifying comparisons between different magnetic unit cells. Fe and O are essentially stationary in the modes considered, meaning force constants between Fe-Fe,Fe-O and O-O atoms do not contribute. La-La and La-O force constants are essentially unchanged in each calculation, and the bond distance between La-Fe is large and the resulting force constant small. Therefore, we can limit ourselves to the "zz" term for La-As, As-As, and Fe-As force constants. Of these, the Fe-As force constant is the largest by an order of magnitude. Even with these simplifications, there was no clear softening of any specific pair-wise force. This provides additional evidence for T. Yildirim's observation that changes in the phonon modes are due to a complicated renormalization rather than softening of a single pair-wise force. [45] In the non-magnetic calculation the on-site force constants, which are a sum of all pair-wise interactions, are (in eV/Å^2) (11.2,11.2,8.9) for Fe and (10.5,10.5,9.6) for

As. They show significant softening around 10-20% with the introduction of magnetic order, in good agreement with T. Yildirim's work. Small differences on the order of 0.2 eV/Å^2 or less in the on-site force constants are likely from slightly different lattice parameters chosen in our calculations.

6.6 Conclusions

In summary, we have measured the phonon dispersion along (00L) tetragonal phase of LaFeAsO at room temperature, well above the magnetic ordering temperature of 138K. Non-magnetic calculations fail to reproduce the observed splitting between two A_{1g} phonon modes at 22 and 26 meV. Spin-polarized first-principles calculations imposing a number of hypothetical antiferromagnetic orders are qualitatively similar and in better agreement with the experimental results than non-spin-polarized calculations. The presence of Fe-spins are necessary to predict the observed spectrum above T_N, however the renormalization of the force constants is quite complex and cannot be reduced to a single pair-wise force constant.

6.7 Acknowledgments

Work at the Ames Laboratory was supported by the Department of Energy-Basic Energy Sciences under Contract No. DE-AC02-07CH11358. Use of the Advanced Photon Source, an Office of Science User Facility operated for the U.S. Department of Energy (DOE) Office of Science by Argonne National Laboratory, was supported by the U.S. DOE under Contract No. DE-AC02-06CH11357. The construction of HERIX was partially supported by the NSF under Grant No. DMR-0115852.

CHAPTER 7. Calculated elastic constants and temperature dependent phonon dispersion of HCP and BCC beryllium

A paper on this subject is in preparation

S. E. Hahn,[1,2] S. Arapan,[3] O. Eriksson,[3] and B. N. Harmon,[1,2]

7.1 Introduction

Beryllium is a potentially toxic but important commercial element, widely used as a hard, lightweight and nonmagnetic material in the defense and aerospace industries as well as for radiation windows and neutron reflectors for particle physics[83] and nuclear fusion experiments[84]. Despite its simple electron configuration, the bulk material has an interesting phase diagram that has generated considerable interest for many years including the present day. Beryllium's crystal structure is hexagonal closed packed (HCP) up to 1530$\pm$10K, before undergoing a structural phase transition to body centered cubic (BCC). The material melts almost immediately after the BCC phase transition at 1560K[85]. Calculations suggest an additional structural transition to FCC[86] or BCC[87, 88, 4] under pressure, but nothing has been observed repeatably up to 180GPa[89, 90]. Phonons in the low-temperature HCP phase are well-described by traditional first principles calculations using the small displacement method. In the BCC structure however, imaginary frequencies appear near the N-point[88, 4]. While not surprising considering the structural transition with temperature, such calculations poorly describe phonons in the BCC structure. Conventional first principle methods for calculating lattice

[1]Department of Physics and Astronomy, Iowa State University, Ames, IA, 50011, USA
[2]Division of Materials Science and Engineering, Ames Laboratory US-DOE, Iowa State University, Ames, IA 50011, USA
[3]Department of Physics and Astronomy, Division of Materials Theory, Uppsala University, Box 516, SE-751210, Uppsala, Sweden, EU

dynamics cannot accurately calculate high temperature thermophysical properties of materials with entropically stabilized modes, limiting theoretical work. In this paper we use a relatively new approach called self-consistent *ab initio* lattice dynamics (SCAILD) to go beyond what is capable with traditional approaches and study the HCP to BCC transition in beryllium.

7.2 HCP Structure

7.2.1 Elastic Constants and Thermal Expansion

First, we attempted to calculate the elastic constants and phonon dispersion in the HCP structure and compare our results to other calculations and measurements in the literature. To estimate temperature dependence, the thermal expansion was calculated according to ref. [91]. The thermal expansion coefficients $\alpha_a = \frac{1}{a}\frac{da}{dT}$, $\alpha_c = \frac{1}{c}\frac{dc}{dT}$ and $\beta = \frac{1}{V}\frac{dV}{dT}$ can be expressed in terms of the elastic constants and partial derivatives of the free energy

$$\alpha_a = \frac{1}{3V(B_{11}B_{12} - B_{12}^2)}\left[-(B_{22}+B_{12})\frac{\partial^2 F^*}{\partial T \partial \epsilon_v} + (B_{12}+B_{11})\frac{\partial^2 F^*}{\partial T \partial \epsilon_c}\right] \tag{7.1}$$

$$\alpha_c = \frac{1}{3V(B_{11}B_{12} - B_{12}^2)}\left[-(B_{22}-2B_{12})\frac{\partial^2 F^*}{\partial T \partial \epsilon_v} + (B_{12}-2B_{11})\frac{\partial^2 F^*}{\partial T \partial \epsilon_c}\right] \tag{7.2}$$

$$\beta = \frac{1}{V(B_{11}B_{12} - B_{12}^2)}\left[-B_{22}\frac{\partial^2 F^*}{\partial T \partial \epsilon_v} + B_{12}\frac{\partial^2 F^*}{\partial T \partial \epsilon_c}\right] \tag{7.3}$$

where $B_{11} = \frac{2}{9}\left(C_{11} + C_{12} + \frac{1}{2}C_{33} + 2C_{13}\right)$, $B_{22} = \frac{2}{9}\left(C_{11} + C_{12} + 2C_{33} - 4C_{13}\right)$, and $B_{12} = \frac{1}{9}\left(C_{33} + C_{13} + 2C_{11} - 4C_{12}\right)$. Volume and tetragonal strains are defined by $\epsilon_v \equiv d\left[\ln\left(V\right)\right]$ and $\epsilon_c \equiv d\left[\ln\left(c/a\right)\right]$. $F^* = F^{ph} + F^{el}$ is the sum of phonon and electron excitation free energies, respectively. The energy of the static lattice is temperature-independent and does not contribute. Zero point motion is included in the phonon free energy. The electron excitation free energy was calculated by the approximate expression given by Sommerfeld and Frank[92],

$$F^{el}(\bar{\epsilon}, T) = -\frac{(\pi k_B)^2}{6} D(\epsilon_F, \bar{\epsilon}) T^2 \tag{7.4}$$

The phonon free energy in the quasi-harmonic approximation is given by, for example, Ref. [93]

$$F^{phon}(\bar{\epsilon}, T) = \int_0^\infty d\omega g(\omega, \bar{\epsilon}) \left[\frac{\hbar\omega}{2} + k_B T \ln(1 - \exp\left(-\hbar\omega/k_B T\right))\right] \tag{7.5}$$

While differentiating the free energy with respect to temperature is straightforward, differentiating with respect to ϵ_c and ϵ_v lacks an analytical expression and is best estimated numerically. The phonon density of states, $g(\omega, \bar{\epsilon})$ and the electronic density of states at ϵ_F, $D(\epsilon_F, \bar{\epsilon})$, were calculated for several different values of the volume ($\epsilon_v = 0.0, \pm 0.018$) and c/a ($\epsilon_c = 0.0, \pm 0.006$). The free energy at a given temperature T was then calculated and a linear fit used to estimate the derivative.

The elastic constants necessary to calculate thermal expansion can be determined by calculating the total energy of the crystal for a series of small distortions. The Taylor series expansion for the total energy with respect to the distortion parameters α_i is

$$E(V, \alpha) = E(V_0, 0) + V_0 \left(\sum_{i=1}^{6} \tau_i \alpha_i \xi_i + \frac{1}{2} \sum_{i=1,j=1}^{6,6} C_{ij} \alpha_i \xi_i \alpha_j \xi_j \right) \tag{7.6}$$

The distortion matrix is symmetric, leading to 6 (rather than 9) unique constants. Voigt notation was used to reduce the number of indices. In this notation xx is replaced by 1, yy by 2, zz by 3, yz and zy by 4, xz and zx by 5, and xy and yx by 6. To ensure off-diagonal terms are properly counted, $\xi = 1$ if the Voigt index is 1,2, or 3 and $\xi = 2$ if the Voigt index is 4, 5 or 6. Materials with hexagonal symmetry have five independent elastic constants, $C_{11}, C_{12}, C_{13}, C_{33}$, and C_{55}. Determining the elastic constants therefore requires five different strains. We used the following distortion matrices multiplied by the lattice vectors to determine the elastic constants of HCP beryllium. The first distortion stretches the crystal in the $x-y$ plane while maintaining hexagonal symmetry. The distortion matrix is

$$\mathbf{e_1} = \begin{pmatrix} 1+\alpha & 0 & 0 \\ 0 & 1+\alpha & 0 \\ 0 & 0 & 1 \end{pmatrix}$$

and the energy associated with this distortion is

$$E(V, \alpha) = E(V_0, 0) + V_0 \left[(\tau_1 + \tau_2)\alpha + (C_{11} + C_{12})\alpha^2 \right] \tag{7.7}$$

The second distortion stretches the crystal in the $x - y$ plane while breaking hexagonal symmetry. The distortion matrix is written as

$$\mathbf{e_2} = \begin{pmatrix} 1+\alpha & 0 & 0 \\ 0 & 1-\alpha & 0 \\ 0 & 0 & 1 \end{pmatrix}$$

and the energy associated with this distortion is

$$E(V,\alpha) = E(V_o,0) + V_o\left[(\tau_1-\tau_2)\alpha + (C_{11}-C_{12})\alpha^2\right] \tag{7.8}$$

Together the first two distortions can be used to determine C_{11} and C_{12}. The third distortion stretches the z-axis and is written as

$$\mathbf{e_3} = \begin{pmatrix} 1 & 0 & 0 \\ 0 & 1 & 0 \\ 0 & 0 & 1+\alpha \end{pmatrix}$$

The energy associated with this distortion is

$$E(V,\alpha) = E(V_0,0) + V_0\left[\tau_3\alpha + \frac{C_{33}}{2}\alpha^2\right] \tag{7.9}$$

and can be used to determine C_{33}. The fourth distortion is written as

$$\mathbf{e_4} = \begin{pmatrix} 1 & 0 & \alpha \\ 0 & 1 & 0 \\ \alpha & 0 & 1 \end{pmatrix}$$

and the energy associated with this distortion is

$$E(V,\alpha) = E(V_0,0) + V_0\left[\tau_5\alpha + 2C_{55}\alpha^2\right] \tag{7.10}$$

This strain can be used to determine C_{55}. The fifth and final distortion is related to the bulk modulus and is written as

$$\mathbf{e_5} = \begin{pmatrix} 1+\alpha & 0 & 0 \\ 0 & 1+\alpha & 0 \\ 0 & 0 & 1+\alpha \end{pmatrix}$$

and the energy associated with this distortion is

$$E(V,\alpha) = E(V_0,0) + V_0\left[(\tau_1+\tau_2+\tau_3)\,\alpha + \frac{1}{2}\left(2C_{11}+2C_{12}+4C_{13}+C_{33}\right)\alpha^2\right] \tag{7.11}$$

The total energy was calculated for $\alpha = [0.00, \pm0.01, \pm0.02, \pm0.03, \pm0.04, \pm0.05]$ and fit to a third order polynomial. These five equations were then solved for the elastic constants C_{ij} and the results are given in the first line of Tbl. 7.1. We also repeated this calculation, allowing the atoms in each distorted structure to relax to the position minimizing the internal forces.

Ab initio calculations were performed with VASP 4 [94, 95, 96, 97] using PAW pseudopotentials[98, 99] and utilizing the PBE exchange-corrrelation functional[100, 101]. After testing convergence of the calculation, an energy cutoff of 350eV and 18x18x12 Gamma centered k-point mesh were chosen to ensure the precision of the calculated elastic constants. Due to forces being calculated, Gaussian smearing with σ=0.2eV was used. The initial lattice parameters of a=2.25546 Å and and c=3.5646 Å were determined from relaxing the lattice parameters to the minimum total energy. These calculations are in good agreement with the experimental lattice parameters of a=2.2866 Å and c=3.5831 Å at 295K[102].The resulting calculated elastic constants are given on the first line of Tbl. 7.1. In addition, distortions associated with C_{11}, C_{12} and C_{55} lead to structures with internal forces on individual atoms. Relaxing the atoms so that all forces are zero improves agreement for C_{11}, though not C_{12} or C_{55}. Results are given in the second line of Tbl. 7.1. Both calculations are in good agreement with recent theoretical work by Leu et al.[4] with small differences likely due to their choice of the LDA (versus PBE) exchange-correlation functional.

7.2.2 Phonon Dispersion

For each value of the volume and c/a, phonon calculations were performed with the small displacement method, described in section 3.2. Two atomic displacements were used to calculate force constants in a 5x5x3 supercell and the phonon density of states was calculated on an 80x80x80 point grid.

Fig. 7.1 shows the calculated thermal expansion, along with measurements by R. W.

Table 7.1 Calculated and measured elastic constants of HCP beryllium. The first two rows are from this work and are in good agreement with recent theoretical work by Leu et al.[4] as well as several experimental measurements.

	C_{11}	C_{12}	C_{13}	C_{33}	C_{55}
Distort cell	323.9	26.0	17.1	374.6	161.6
Relax atoms	308.6	41.3	17.1	374.6	158.4
Luo et al. (thy)[4]	310.9	19.5	19.1	359.5	162.1
A Migliori et al.[103]	293.6	26.8	14.0	356.7	162.2
J F Smith et al.[104]	299.4	27.6	11.0	342.2	166.2
L. Gold[105]	308	-58	87	357	110
Fisher, Dever[106]	294.0	26.7	14.0	336.4	162.5
Silversmith, Averbach[107]	295.4	27.6	14.2	357.0	163.0
Testardi, Condon[108]	285.8	14.8	11.0	354.2	166.9

Meyerhoff and J. F. Smith[6]. There is good agreement between theory and experiment through 270K. The second phonon dispersion shown in Fig. 7.2 was recalculated using lattice parameters (a=2.26425Å, c=3.57505Å)calculated from the thermal expansion at 500K. The experimental data points were measured at 80K by R. Stedman, et al. [7]. Considering the use of theoretical lattice parameters, overall agreement between theory and experiment is quite good. Changes in the lattice parameters from thermal expansion has a very minor effect on the phonon dispersion.

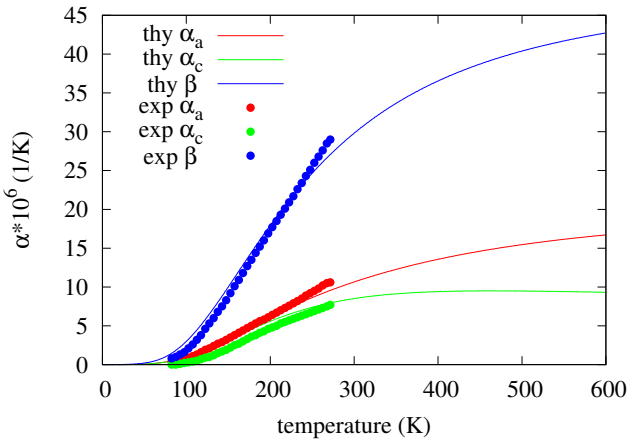

Figure 7.1 Calculated thermal expansion of HCP beryllium up to 600K. Measurements up the 270K are by R. W. Meyerhoff and J. F. Smith[6].

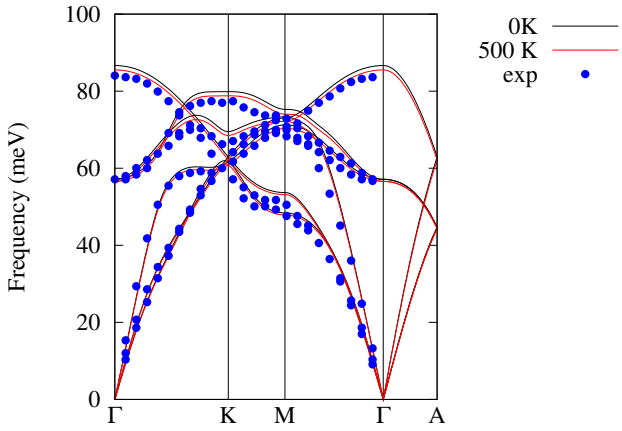

Figure 7.2 Calculated phonon dispersion of HCP beryllium. The black and red lines use the calculated lattice parameters at 0K and 500K, respectively. The blue data points were measured at 80K by R. Stedman, et al. [7]

7.3 BCC Structure

7.3.1 SCAILD

Unlike the HCP structure, phonon calculations of the BCC structure using the small displacement method, shown in black on Fig. 7.3, have imaginary modes near the N-point. While not surprising considering the structural transition with temperature, this calculation poorly describes phonons in the BCC structure. Motion consistent with the N-point (110) phonon along with a shear distortion transforms it from a BCC to a HCP structure[109]. The SCAILD method goes beyond the harmonic approximation to include phonon-phonon interactions and produces a temperature-dependent phonon dispersion. It has been used to study many different systems, including the $\alpha \rightarrow \beta$ transition in Ti, Zr and Hf[110, 111], NiTi[112], ZrO_2[113], and Fe in the earth's core[114].

Additional BCC calculations were performed using the SCAILD code written by Petros Souvatzis[111, 115]. Here we will only consider a monoatomic lattice which simplifies the notation and applies to this specific calculation. The straightforward extension of the SCAILD method for crystals structures with multiple atoms per unit cell is described elsewhere[113].

In chapter 3, solving the equation of motion classically was sufficient to understand the small displacement method. Solving the same equation with quantum mechanics, we introduce

the canonical phonon coordinates $\mathcal{Q}_{\mathbf{k}s}$ and $\mathcal{P}_{\mathbf{k}s}$. The operators $\mathbf{P_R}$ and $\mathbf{U_R}$ can be expressed as

$$\mathbf{U_R} = \frac{1}{\sqrt{MN}} \sum_{\mathbf{q}s} \mathcal{Q}_{\mathbf{q}s} \epsilon_{\mathbf{q}s} e^{i\mathbf{q}\cdot\mathbf{R}} \tag{7.12}$$

$$\mathbf{P_R} = \frac{1}{\sqrt{MN}} \sum_{\mathbf{q}s} \mathcal{P}_{\mathbf{q}s} \epsilon_{\mathbf{q}s} e^{i\mathbf{q}\cdot\mathbf{R}} \tag{7.13}$$

where $\epsilon_{\mathbf{k}s}$ is the phonon eigenvector associated with branch s at wavevector $\mathbf{k}$, M is the atomic mass, N is the number of atoms, and R is the real space lattice vector. With this substitution, the Hamiltonian turns into 3N independent harmonic oscillators. The mean squared atomic displacements are given by

$$\left\langle \mathcal{Q}^{\dagger}_{\mathbf{q}s} \mathcal{Q}_{\mathbf{q}s} \right\rangle = \frac{\hbar}{\omega_{\mathbf{q}s}} \left[\frac{1}{2} + n\left(\frac{\hbar\omega_{\mathbf{q}s}}{k_B T} \right) \right] \tag{7.14}$$

where $\omega_{\mathbf{q}s}$ is the phonon eigenvalue and $n(x)$ is the Bose occupation. In the classical limit, operators in Eqn. 7.14 are replaced by real numbers divided by the mass and the + or - sign chosen randomly.

$$\mathcal{A}_{\mathbf{q}s} = \pm \sqrt{\frac{\left\langle \mathcal{Q}^{\dagger}_{\mathbf{q}s} \mathcal{Q}_{\mathbf{q}s} \right\rangle}{M}} \tag{7.15}$$

The displacements for all phonon modes commensurate with the supercell are then calculated from Eqn. 7.12. The Hellmann-Feynman forces on each atom are calculated by VASP or another first principles code. A set of new phonon frequencies can be calculated from the Fourier transform of the forces, $\mathbf{F_q}$

$$\omega_{\mathbf{q}s} = \left[-\frac{1}{M} \frac{\epsilon_{\mathbf{q}s} \cdot \mathbf{F_q}}{\mathcal{A}_{\mathbf{q}s}} \right]^{1/2} \tag{7.16}$$

From these expressions an iterative procedure can be created as follows:

1. An initial set of phonon frequencies and eigenvectors are required. This typically comes from a phonon calculation using the small displacement method.

2. Eqns. 7.15 and 7.12 with $\mathcal{Q}/\sqrt{M} \rightarrow \mathcal{A}$ are then used to determine displacements of each atom from all phonon modes commensurate with the supercell.

3. After moving the atoms in a supercell according to these displacements, a first principles code is then used to calculate the Hellmann-Feynman forces on each atom.

4. Phonon frequencies are recalculated from the Fourier transform of the calculated forces using Eqn. 7.16.

5. These frequencies are fed into step 2 and the process repeated until the average dispersion or other quantity of interest converges to a fixed value.

In practice, two additional steps are required at the end of each iteration. First, symmetry is restored at the end of each iteration using Eqn. 7.17

$$\Omega^2_{\mathbf{q}s}(i) = \frac{1}{m_{\mathbf{q}}} \sum_{S \in S(\mathbf{q})} \omega^2_{S^{-1}\mathbf{q}S}(i) \tag{7.17}$$

In addition, the frequencies are averaged over all or a subset of previous iterations, where the number of iterations saved can affect convergence.

$$\omega^2_{\mathbf{q}s}(N_I) = \frac{1}{N_I} \sum_{i=1}^{N_I} \Omega^2_{\mathbf{q}s}(i) \tag{7.18}$$

BCC calculations were performed at the experimental lattice parameter at 1533K, 2.552Å[102]. A 4x4x4 k-point mesh in a 4x4x4 supercell (equivalent to 16x16x16 in the Brillouin zone), and a 400 eV energy cutoff were used. Fermi-Dirac smearing was set to the same temperature used in the SCAILD calculation (1533K=0.1321eV). The resulting phonon dispersion is shown in Fig. 7.3. The largest differences are hardening of phonon frequencies at the P-point and stabilizing the N-point phonon mode. Similar changes were observed in Ti, Zr and Hf[111] We ran calculations of the phonon dispersion down to 300K, and while the N-point mode softened substantially, it was still real. At the time of this investigation, it was clear that expressions for the phonon free energy from the quasi-harmonic approximation, such as Eqn. 7.5, cannot be accurately used in SCAILD calculations. A proposed solution is under development[110].

7.3.2 Fitting Elastic Constants

To avoid these issues with the phonon free energy, fits to the calculated phonon dispersion were used to determine the the elastic constants in the BCC phase. Elastic Constants were

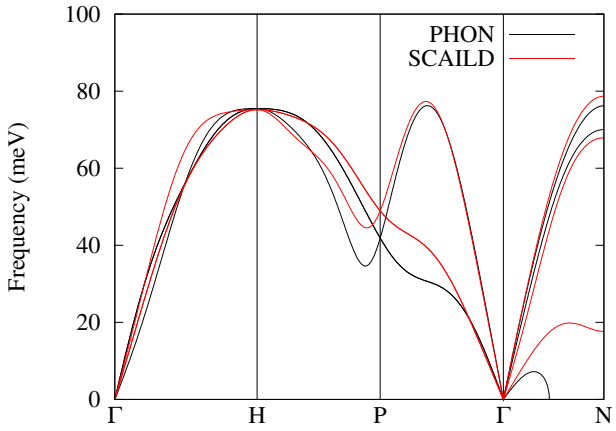

Figure 7.3 Phonon dispersion of BCC beryllium. The black lines are a 0K calculation using the small displacement method. The red lines are a SCAILD calculation at 1533K.

determined from the Christoffel Equation, given in Eqn. 7.19 in much the same way it is from neutron and x-ray scattering measurements at small-**q** near the zone-center.

$$\rho\left(\omega/q\right)^2 \mathbf{A} = \mathbf{Ch}\ \mathbf{A} \tag{7.19}$$

Here ω is the phonon frequency at and q the magnitude of **q**, and **A** is a polarization vector. The general case is given in [39, 116]. Here we will only repeat simplified expressions for the cubic and hexagonal symmetries necessary for these materials. Crystals with cubic symmetry have three independent parameters: C_{11},C_{12},and C_{44}. In this case, **Ch** reduces to

$\mathbf{Ch}_{\text{cubic}}=$

$$\begin{bmatrix} C_{11}n_1^2 + C_{44}\left(n_2^2+n_3^2\right) & \left(C_{12}+C_{44}\right)n_1n_2 & \left(C_{12}+C_{44}\right)n_3n_1 \\ \left(C_{12}+C_{44}\right)n_2n_1 & C_{11}n_2^2 + C_{44}\left(n_3^2+n_1^2\right) & \left(C_{12}+C_{44}\right)n_2n_3 \\ \left(C_{12}+C_{44}\right)n_3n_1 & \left(C_{12}+C_{44}\right)n_2n_3 & C_{11}n_3^2 + C_{44}\left(n_1^2+n_2^2\right) \end{bmatrix}$$

where $n_i = \mathbf{q_i}/|\mathbf{q}|$. Hexagonal symmetry has 5 independent parameters: C_{11}, C_{12},C_{13},C_{33}, and C_{55}. In this case, **Ch** reduces to

$\mathbf{Ch}_{\text{hexagonal}}=$

$$\begin{bmatrix} C_{11}\left(n_1^2+\frac{n_2^2}{2}\right) - C_{12}n_2^2 + C_{55}n_3 & \left(C_{11}+C_{12}\right)\frac{n_1n_2}{2} & \left(C_{13}+C_{55}\right)n_1n_3 \\ \left(C_{11}+C_{12}\right)\frac{n_2n_1}{2} & C_{11}\left(\frac{n_1^2}{2}+n_2^2\right) - C_{12}n_1^2 + c_{44}n_3^2 & \left(C_{13}+C_{55}\right)n_2n_3 \\ \left(C_{13}+C_{55}\right)n_3n_1 & \left(C_{13}+C_{55}\right)n_2n_3 & C_{33}n_3^2 + C_{55}\left(n_1^2+n_2^2\right) \end{bmatrix}$$

Given samples of the phonon dispersion in different directions, elastic constants can be fit to this set of equations. C_{11} and C_{12} and C_{55} was fit to 11 samples of the three non-degenerate acoustic modes along ($\Gamma \rightarrow K$) and C_{33} and C_{55} were fit to 11 samples of the two non-degenerate acoustic modes along ($\Gamma \rightarrow A$).

Table 7.2 Elastic constants (in GPa) of HCP beryllium from fits to the calculated phonon dispersion at 0K. Calculated elastic constants from total energy calculations are included for reference.

	C_{11}	C_{12}	C_{33}	C_{55}
distortions	308.6	41.3	374.6	158.4
3x3x2	294.7	-22.4	282.7	158.8
5x5x3	247.8	-33.4	328.2	157.1
6x6x4	269.0	-15.0	335.1	164.3

While fitted values lack the precision of the those calculated from small distortions of the unit cell, values are similar and the accuracy of phonon modes at small **q** should improve with supercell size. The same method can be applied to SCAILD calculations of the BCC phase. C_{11}, C_{12} and C_{44} were fit to 11 samples of three non-degenerate acoustic modes along ($\Gamma \rightarrow N$). A recently published method for determining the free energy from SCAILD calculations[110] may help improve the precision of the calculated elastic constants and theoretically determine the transition temperature.

Table 7.3 Elastic constants (in GPa) of BCC beryllium from fits to the calculated phonon dispersion at 1533K.

	C_{11}	C_{12}	C_{44}
Fit	44.0	28.0	27.2
Converted[103]	281.5	23.9	148.3

A. Migliori et al converted the BCC elastic constants from HCP measurements by equating the bulk modulus, the three values of ρv^2 (where ρ is the mass density and v is the sound velocity), and the two shear-elastic-constant anisotropies.[103] Fitted values of C_{11} and C_{44} are an order of magnitude smaller than the converted values. This suggests the elastic moduli, and consequently the bonding, is substantially different in the BCC structure than in the lower-temperature HCP phase.

7.4 Conclusions

In conclusion, the phonon dispersion and elastic constants in HCP Beryllium are well described by first-principles calculations using the small displacement method. Phonon-phonon interactions dynamically stabilize the N-point phonon in the high temperature BCC structure. Lastly, fits to the calculated phonon dispersion were used to surmount the difficulties of accurately calculating the free energy and estimating the elastic constants in the BCC phase.

CHAPTER 8. Conclusion

The discovery of iron-based superconductors in 2008 created a very exciting time to be studying physics. New and exciting experimental discoveries are being published regularly and our theory group has made important contributions. While superconductivity in these compounds does not originate from conventional electron-phonon coupling, these systems do display significant sensitivity to the lattice geometry. Theoretical studies have shown that strong coupling between Fe magnetism and the As position leads to the softening of the Fe-As force constants. We have carefully studied specific phonon modes in $CaFe_2As_2$ and LaFeAsO, to better understand these effects.

In the first study (Chapter 5), we have measured the phonon dispersion along several high symmetry directions for the paramagnetic high temperature tetragonal phase of $CaFe_2As_2$. Spin-polarized first principles calculations are in better agreement with the experimental results than non-spin-polarized calculations. The effects of large theoretical magnetic moments and the details of the spin fluctuations at room temperature are issues still under investigation.

In the second study (Chapter 6), we have measured the phonon dispersion along (0,0,L) in the tetragonal phase of LaFeAsO at room temperature, well above the magnetic ordering temperature of 138K. Nonmagnetic calculations fail to reproduce the observed splitting between two A_{1g} phonon modes at 22 and 26 meV. Spin-polarized first-principles calculations imposing a number of hypothetical antiferromagnetic orders are qualitatively similar and in better agreement with the experimental results than non-spin-polarized calculations. The presence of Fe-spins are necessary to predict the observed spectrum above T_N, however the renormalization of the force constants is quite complex and cannot be reduced to a single pair-wise force constant.

In our final study, we utilized a relatively new approach called self- consistent *ab ini-*

tio lattice dynamics (SCAILD), which goes beyond the harmonic approximation to include phonon-phonon interactions and produce a temperature-dependent phonon dispersion. The phonon dispersion and elastic constants in HCP Beryllium are well described by first-principles calculations using the small displacement method. Phonon-phonon interactions dynamically stabilize the N-point phonon in the high temperature BCC structure. Lastly, fits to the calculated phonon dispersion were used to surmount difficulties of accurately calculating the free energy and estimate the elastic constants in the BCC phase.

APPENDIX A. Force Constants in LaFeAsO

We investigated the real-space force constants associated with these two A_{1g} modes. Considering only z-polarized phonon branches containing La and As motion significantly reduces the number of force constants that contribute. First, only the "zz" term in the 3x3 force constant tensor can contribute, greatly simplifying comparisons between different magnetic unit cells. Fe and O are essentially stationary, meaning these force constants between Fe-Fe,Fe-O and O-O atoms do not contribute. La-La and La-O force constants are essentially unchanged in each calculation, and the bond distance between La-Fe is greater than nearest neighbor, and weak. Therefore, we can limit ourselves to the "zz" term for La-As, As-As, and Fe-As force constants. Of these, the Fe-As force constant is largest by an order of magnitude. In the tetragonal checkerboard magnetic structure, the Fe-As force constant softens by 20%. This pattern, however, does not continue into the two orthorhombic space groups. With SDW and striped ordering, the Fe-As force constant only softens by 2% and 0.5%, respectively. As-As force constants above/below the Fe plane change sign from negative to positive. In the checkerboad pattern, the magnitude doubles, while in the SDW and stripe pattern, the magnitude is halved. The orthorhombic space group, however, breaks the symmetry along orthorhombic A_o (1,1,0) and B_o (1,-1,0). For the bond along A_o and L_o, the La-As force constant stiffens by $\sim$300%, with only small changes in the force constant associated with the bond along B_o. In the checkerboard pattern, this force constant stiffens by 140%, but is equal along A_o and B_o.

Considering differences in the bonds along A_o and B_o, it is also interesting to investigate changes in the Fe-Fe force constants. Along A_o in the SDW and striped ordering, the "zz" force constant is positive. By contrast, along B_o the "zz" force constant is negative. In the checkerboard order, the force constant is smaller in magnitude by 23%, but in the same direction for bonds along A_o and B_o. Imposing a tetragonal space group appears to average out some

anisotropic force constants. While softening the Fe-As force constant does soften the A_{1g} in the tetragonal structure, the difference in the force constants for bonds along A_o and B_o achieve similar results in the magnetic structures with orthorhombic space groups.

BIBLIOGRAPHY

[1] D. Waasmaier and A. Kirfel. New analytical scattering-factor functions for free atoms and ions. *Acta Crystallographica Section A*, 51(3):416–431, May 1995.

[2] Y. Kamihara, T. Watanabe, M. Hirano, and H. Hosono. Iron-based layered superconductor $LaO_{1-x}F_xFeAs$ (x = 0.05-0.12) with T_c = 26 K. *Journal of the American Chemical Society*, 130(11):3296–3297, 2008.

[3] D. C. Johnston. The puzzle of high temperature superconductivity in layered iron pnictides and chalcogenides. *Advances in Physics*, 59(6):803–1061, 2010.

[4] F. Luo, L.-C. Cai, X.-R. Chen, F.-Q. Jing, and D. Alfè. Ab initio calculation of lattice dynamics and thermodynamic properties of beryllium. *Journal of Applied Physics*, 111(5):053503, 2012.

[5] W. Quester. This work has been released into the public domain by its author. `http://en.wikipedia.org/wiki/File:Sketch_Pseudopotentials.png`.

[6] R. W. Meyerhoff and J. F. Smith. Anisotropic thermal expansion of single crystals of thallium, yttrium, beryllium, and zinc at low temperatures. *Journal of Applied Physics*, 33(1):219–224, 1962.

[7] R. Stedman, Z. Amilius, R. Pauli, and O. Sundin. Phonon spectrum of beryllium at 80K. *Journal of Physics F: Metal Physics*, 6(2):157, 1976.

[8] Y. Lee. First principles calculations for x-ray resonant spectra and elastic properties. Master's thesis, Iowa State University, 2004.

[9] R. G. Hennig. Ab-initio methods of electronic structure. `http://theory.mse.cornell.edu/Notes-PASI2012.pdf`, June 2012.

[10] P. A. M. Dirac. Quantum Mechanics of Many-Electron Systems. *Royal Society of London Proceedings Series A*, 123:714–733, April 1929.

[11] P. Hohenberg and W. Kohn. Inhomogeneous electron gas. *Phys. Rev.*, 136:B864–B871, Nov 1964.

[12] W. Kohn and L. J. Sham. Self-consistent equations including exchange and correlation effects. *Phys. Rev.*, 140:A1133–A1138, Nov 1965.

[13] L. J. Sham and W. Kohn. One-particle properties of an inhomogeneous interacting electron gas. *Phys. Rev.*, 145:561–567, May 1966.

[14] D. M. Ceperley and B. J. Alder. Ground state of the electron gas by a stochastic method. *Phys. Rev. Lett.*, 45:566–569, Aug 1980.

[15] L. Hedin and B. I. Lundqvist. Explicit local exchange-correlation potentials. *Journal of Physics C: Solid State Physics*, 4(14):2064, 1971.

[16] U. von Barth and L. Hedin. A local exchange-correlation potential for the spin polarized case. *Journal of Physics C: Solid State Physics*, 5(13):1629, 1972.

[17] J. P. Perdew and A. Zunger. Self-interaction correction to density-functional approximations for many-electron systems. *Phys. Rev. B*, 23:5048–5079, May 1981.

[18] S. H. Vosko, L. Wilk, and M. Nusair. Accurate spin-dependent electron liquid correlation energies for local spin density calculations: a critical analysis. *Canadian Journal of Physics*, 58(8):1200–1211, 1980.

[19] S. Goedecker, M. Teter, and J. Hutter. Separable dual-space gaussian pseudopotentials. *Phys. Rev. B*, 54:1703–1710, Jul 1996.

[20] J. P. Perdew and Y. Wang. Accurate and simple analytic representation of the electron-gas correlation energy. *Phys. Rev. B*, 45:13244–13249, Jun 1992.

[21] F. Herman, J. P. Van Dyke, and I. B. Ortenburger. Improved statistical exchange approximation for inhomogeneous many-electron systems. *Phys. Rev. Lett.*, 22:807–811, Apr 1969.

[22] P. S. Svendsen and U. von Barth. Gradient expansion of the exchange energy from second-order density response theory. *Phys. Rev. B*, 54:17402–17413, Dec 1996.

[23] Y. Wang and J. P. Perdew. Correlation hole of the spin-polarized electron gas, with exact small-wave-vector and high-density scaling. *Phys. Rev. B*, 44:13298–13307, Dec 1991.

[24] J. P. Perdew, K. Burke, and M. Ernzerhof. Generalized gradient approximation made simple. *Phys. Rev. Lett.*, 77(18):3865–3868, Oct 1996.

[25] D. J. Singh and L. Nordström. *Planewaves, Pseudopotentials, and the LAPW Method*. Springer Science+Business Media, Inc., second edition, 2006.

[26] N. W. Ashcroft and N. Mermin. *Solid State Physics*. Holt, Rinehart and Winston, 1976.

[27] R. Cohen. Lattice dynamics, thermal properties, and density functional perturbation theory. `http://flash.atlas.illinois.edu/video.html?src=/mcc/mcc-v-2009-1/12IntroductionToLatticeDynamicsandThermanlPropertiesofSolids&player=SDNC`, June 2012.

[28] D. Alfè. Phon: A program to calculate phonons using the small displacement method. *Computer Physics Communications*, 180(12):2622–2633, 2009.

[29] R. P. Feynman. Forces in molecules. *Phys. Rev.*, 56:340–343, Aug 1939.

[30] S. Baroni, S. de Gironcoli, A. Dal Corso, and P. Giannozzi. Phonons and related crystal properties from density-functional perturbation theory. *Rev. Mod. Phys.*, 73:515–562, Jul 2001.

[31] R. M. Sternheimer. Electronic polarizabilities of ions from the hartree-fock wave functions. *Phys. Rev.*, 96:951–968, Nov 1954.

[32] A. Q. R. Baron. *Journal of The Spectroscopical Society of Japan*, 58(5):205–204, 2009.

[33] A. H. Said, H. Sinn, and R. Divan. New developments in fabrication of high-energy-resolution analyzers for inelastic X-ray spectroscopy. *Journal of Synchrotron Radiation*, 18(3):492–496, May 2011.

[34] T. S. Toellner, A. Alatas, and A. H. Said. Six-reflection meV-monochromator for synchrotron radiation. *Journal of Synchrotron Radiation*, 18(4):605–611, Jul 2011.

[35] E. Burkel. Phonon spectroscopy by inelastic x-ray scattering. *Reports on Progress in Physics*, 63(2):171, 2000.

[36] S. W. Lovesey. *Theory of Neutron Scattering From Condensed Matter*, volume 1 of *International Series of Monographs on Physics*. Oxford University Press, 1984.

[37] G. L. Squires. *Introduction to the Theory of Thermal Neutron Scattering*. Cambridge University Press, 1978.

[38] L. Van Hove. Correlations in space and time and born approximation scattering in systems of interacting particles. *Phys. Rev.*, 95:249–262, Jul 1954.

[39] H. Fukui, T. Katsura, T. Kuribayashi, T. Matsuzaki, A. Yoneda, E. Ito, Y. Kudoh, S. Tsutsui, and A. Q. R. Baron. Precise determination of elastic constants by high-resolution inelastic X-ray scattering. *Journal of Synchrotron Radiation*, 15(6):618–623, Nov 2008.

[40] D. Zaharioudakis. Tetrahedron methods for brillouin zone integration. *Computer Physics Communications*, 157(1):17 – 31, 2004.

[41] P. E. Blöchl, O. Jepsen, and O. K. Andersen. Improved tetrahedron method for brillouin-zone integrations. *Phys. Rev. B*, 49:16223–16233, Jun 1994.

[42] H. J. Monkhorst and J. D. Pack. Special points for brillouin-zone integrations. *Phys. Rev. B*, 13:5188–5192, Jun 1976.

[43] R. Zhi-An, L. Wei, Y. Jie, Y. Wei, S. Xiao-Li, Zheng-Cai, C. Guang-Can, D. Xiao-Li, S. Li-Ling, Z. Fang, and Z. Zhong-Xian. Superconductivity at 55K in iron-based F-doped

layered quaternary compound $SmO_{1-x}F_xFeAs$. *Chinese Physics Letters*, 25(6):2215–2216, 2008.

[44] L. Boeri, O. V. Dolgov, and A. A. Golubov. Is $LaFeAsO_{1-x}F_x$ an electron-phonon superconductor? *Phys. Rev. Lett.*, 101:026403, Jul 2008.

[45] T. Yildirim. Frustrated magnetic interactions, giant magnetoelastic coupling, and magnetic phonons in ironpnictides. *Physica C: Superconductivity*, 469(912):425 – 441, 2009.

[46] A. Kreyssig, M. A. Green, Y. Lee, G. D. Samolyuk, P. Zajdel, J. W. Lynn, S. L. Bud'ko, M. S. Torikachvili, N. Ni, S. Nandi, J. B. Leão, S. J. Poulton, D. N. Argyriou, B. N. Harmon, R. J. McQueeney, P. C. Canfield, and A. I. Goldman. Pressure-induced volume-collapsed tetragonal phase of $cafe_2as_2$ as seen via neutron scattering. *Phys. Rev. B*, 78:184517, Nov 2008.

[47] D. K. Pratt, Y. Zhao, S. A. J. Kimber, A. Hiess, D. N. Argyriou, C. Broholm, A. Kreyssig, S. Nandi, S. L. Bud'ko, N. Ni, P. C. Canfield, R. J. McQueeney, and A. I. Goldman. Suppression of antiferromagnetic spin fluctuations in the collapsed phase of $CaFe_2As_2$. *Phys. Rev. B*, 79:060510, Feb 2009.

[48] R. J. McQueeney, S. O. Diallo, V. P. Antropov, G. D. Samolyuk, C. Broholm, N. Ni, S. Nandi, M. Yethiraj, J. L. Zarestky, J. J. Pulikkotil, A. Kreyssig, M. D. Lumsden, B. N. Harmon, P. C. Canfield, and A. I. Goldman. Anisotropic three-dimensional magnetism in $CaFe_2As_2$. *Phys. Rev. Lett.*, 101(22):227205, 2008.

[49] S. O. Diallo, D. K. Pratt, R. M. Fernandes, W. Tian, J. L. Zarestky, M. Lumsden, T. G. Perring, C. L. Broholm, N. Ni, S. L. Bud'ko, P. C. Canfield, H.-F. Li, D. Vaknin, A. Kreyssig, A. I. Goldman, and R. J. McQueeney. Paramagnetic spin correlations in $CaFe_2As_2$ single crystals. *Phys. Rev. B*, 81:214407, Jun 2010.

[50] M. Ishikado, R. Kajimoto, S.-i. Shamoto, M. Arai, A. Iyo, K. Miyazawa, P. M. Shirage, H. Kito, H. Eisaki, S. Kim, H. Hosono, T. Guidi, R. Bewley, and S. M. Bennington. Evidence of spin density wave in LaFeAsO, the parent material of the new Fe-based oxypnictide superconductors. *ArXiv e-prints*, September 2008.

[51] S. Wakimoto, K. Kodama, M. Ishikado, M. Matsuda, R. Kajimoto, M. Arai, K. Kakurai, F. Esaka, A. Iyo, H. Kito, H. Eisaki, and S. Shamoto. Degradation of superconductivity and spin fluctuations by electron overdoping in lafeaso$_{1-x}$f$_x$. *Journal of the Physical Society of Japan*, 79(7):074715, 2010.

[52] J.-Q. Yan, S. Nandi, J. L. Zarestky, W. Tian, A. Kreyssig, B. Jensen, A. Kracher, K. W. Dennis, R. J. McQueeney, A. I. Goldman, R. W. McCallum, and T. A. Lograsso. Flux growth at ambient pressure of millimeter-sized single crystals of LaFeAsO, LaFeAsO$_{1-x}$F$_x$, and LaFe$_{1-x}$Co$_x$AsO. *Applied Physics Letters*, 95(22):222504, 2009.

[53] T. Fukuda, A. Q. R. Baron, S. Shamoto, M. Ishikado, H. Nakamura, M. Machida, H. Uchiyama, S. Tsutsui, A. Iyo, H. Kito, J. Mizuki, M. Arai, H. Eisaki, and H. Hosono. Lattice dynamics of LaFeAsO$_{1-x}$F$_x$ and PrFeAsO$_{1-y}$ via inelastic x-ray scattering and first-principles calculation. *Journal of the Physical Society of Japan*, 77(10):103715, 2008.

[54] D. Reznik, K. Lokshin, D. C. Mitchell, D. Parshall, W. Dmowski, D. Lamago, R. Heid, K.-P. Bohnen, A. S. Sefat, M. A. McGuire, B. C. Sales, D. G. Mandrus, A. Subedi, D. J. Singh, A. Alatas, M. H. Upton, A. H. Said, A. Cunsolo, Yu. Shvyd'ko, and T. Egami. Phonons in doped and undoped bafe$_2$as$_2$ investigated by inelastic x-ray scattering. *Phys. Rev. B*, 80:214534, Dec 2009.

[55] R. Mittal, L. Pintschovius, D. Lamago, R. Heid, K.-P. Bohnen, D. Reznik, S. L. Chaplot, Y. Su, N. Kumar, S. K. Dhar, A. Thamizhavel, and Th. Brueckel. Anomalous phonons in CaFe$_2$As$_2$ explored by inelastic neutron scattering. *Journal of Physics: Conference Series*, 251(1):012008, 2010.

[56] I. I. Mazin and M. D. Johannes. A key role for unusual spin dynamics in ferropnictides. *Nature Physics*, 5:141–145, February 2009.

[57] I. I. Mazin and M. D. Johannes. A key role for unusual spin dynamics in ferropnictides. *Nat. Phys.*, 5:141, 2009.

[58] T. Yildirim. Frustrated magnetic interactions, giant magneto-elastic coupling, and magnetic phonons in iron-pnictides. *Physica C: Superconductivity*, 469(9-12):425 – 441, 2009.

[59] R. Mittal, L. Pintschovius, D. Lamago, R. Heid, K-P. Bohnen, D. Reznik, S. L. Chaplot, Y. Su, N. Kumar, S. K. Dhar, A. Thamizhavel, and Th. Brueckel. Measurement of anomalous phonon dispersion of cafe[sub 2]as[sub 2] single crystals using inelastic neutron scattering. *Physical Review Letters*, 102(21):217001, 2009.

[60] R. J. McQueeney. unpublished data.

[61] X. F. Wang, T. Wu, G. Wu, H. Chen, Y. L. Xie, J. J. Ying, Y. J. Yan, R. H. Liu, and X. H. Chen. Anisotropy in the electrical resistivity and susceptibility of superconducting $BaFe_2As_2$ single crystals. *Phys. Rev. Lett.*, 102(11):117005, 2009.

[62] G. M. Zhang, Y. H. Su, Z. Y. Lu, Z. Y. Weng, D. H. Lee, and T. Xiang. Universal linear-temperature dependence of static magnetic susceptibility in iron pnictides. *Europhys. Lett.*, 86(3):37006, 2009.

[63] N. Ni, M. E. Tillman, J.-Q. Yan, A. Kracher, S. T. Hannahs, S. L. Bud'ko, and P. C. Canfield. Effects of co substitution on thermodynamic and transport properties and anisotropic H_{c2} in $Ba(Fe_{1-x}Co_x)_2As_2$ single crystals. *Phys. Rev. B*, 78(21):214515, 2008.

[64] M. A. Tanatar, N. Ni, G. D. Samolyuk, S. L. Bud'ko, P. C. Canfield, and R. Prozorov. Resistivity anisotropy of AFe_2As_2 (A = Ca, Sr, Ba): Direct versus montgomery technique measurements. *Phys. Rev. B*, 79(13):134528, 2009.

[65] N. Ni, S. Nandi, A. Kreyssig, A. I. Goldman, E. D. Mun, S. L. Bud'ko, and P. C. Canfield. First-order structural phase transition in $CaFe_2As_2$. *Phys. Rev. B*, 78(1):014523, 2008.

[66] P.C. Canfield, S.L. Bud'ko, N. Ni, A. Kreyssig, A.I. Goldman, R.J. McQueeney, M.S. Torikachvili, D.N. Argyriou, G. Luke, and W. Yu. Structural, magnetic and superconducting phase transitions in $CaFe_2as_2$ under ambient and applied pressure. *Physica C: Superconductivity*, 469(9-12):404 – 412, 2009.

[67] P. Giannozzi et al. http://www.quantum-espresso.org/.

[68] We used the pseudopotentials Ca.pbe-nsp-van.UPF, Fe.pbe-sp-van_ak.UPF and As.pbe-n-van.UPF from the http://www.quantum-espresso.org distribution.

[69] A. I. Goldman, D. N. Argyriou, B. Ouladdiaf, T. Chatterji, A. Kreyssig, S. Nandi, N. Ni, S. L. Bud'ko, P. C. Canfield, and R. J. McQueeney. Lattice and magnetic instabilities in $CaFe_2As_2$: A single crystal neutron diffraction study. *Phys. Rev. B*, 78:100506(R), 2008.

[70] M. Zbiri, H. Schober, M. R. Johnson, S. Rols, R. Mittal, Y. Su, M. Rotter, and D. Johrendt. Ab initio lattice dynamics simulations and inelastic neutron scattering spectra for studying phonons in $BaFe_2As_2$]: Effect of structural phase transition, structural relaxation, and magnetic ordering. *Phys. Rev. B*, 79(6):064511, 2009.

[71] A. D. Christianson, M. D. Lumsden, O. Delaire, M. B. Stone, D. L. Abernathy, M. A. McGuire, A. S. Sefat, R. Jin, B. C. Sales, D. Mandrus, E. D. Mun, P. C. Canfield, J. Y. Y. Lin, M. Lucas, M. Kresch, J. B. Keith, B. Fultz, E. A. Goremychkin, and R. J. McQueeney. Phonon density of states of $LaFeAsO_{1-x}F_x$. *Phys. Rev. Lett.*, 101:157004, Oct 2008.

[72] S. Higashitaniguchi, M. Seto, S. Kitao, Y. Kobayashi, M. Saito, R. Masuda, T. Mitsui, Y. Yoda, Y. Kamihara, M. Hirano, and H. Hosono. Iron-specific phonon density of states in the superconductors $LaFeAsO_{1-x}F_x$ and $La_{1-x}ca_xFePO$. *Phys. Rev. B*, 78:174507, Nov 2008.

[73] S. E. Hahn, Y. Lee, N. Ni, P. C. Canfield, A. I. Goldman, R. J. McQueeney, B. N. Harmon, A. Alatas, B. M. Leu, E. E. Alp, D. Y. Chung, I. S. Todorov, and M. G. Kanatzidis. Influence of magnetism on phonons in $CaFe_2As_2$ as seen via inelastic x-ray scattering. *Phys. Rev. B*, 79:220511, Jun 2009.

[74] M. Le Tacon, T. R. Forrest, Ch. Rüegg, A. Bosak, A. C. Walters, R. Mittal, H. M. Rønnow, N. D. Zhigadlo, S. Katrych, J. Karpinski, J. P. Hill, M. Krisch, and D. F. McMorrow. Inelastic x-ray scattering study of superconducting $smfeaso_{1-x}f_y$ single crystals: Evidence for strong momentum-dependent doping-induced renormalizations of optical phonons. *Phys. Rev. B*, 80:220504, Dec 2009.

[75] C. de la Cruz, Q. Huang, J. W. Lynn, Jiying Li, W. Ratcliff II, J. L. Zarestky, H. A.

Mook, G. F. Chen, J. L. Luo, N. L. Wang, and Pengcheng Dai. *Nature*, 453:899–902, april 2008.

[76] H.-H. Klauss, H. Luetkens, R. Klingeler, C. Hess, F. J. Litterst, M. Kraken, M. M. Korshunov, I. Eremin, S.-L. Drechsler, R. Khasanov, A. Amato, J. Hamann-Borrero, N. Leps, A. Kondrat, G. Behr, J. Werner, and B. Büchner. Commensurate spin density wave in LaFeAsO: A local probe study. *Phys. Rev. Lett.*, 101:077005, Aug 2008.

[77] P. Giannozzi, S. Baroni, N. Bonini, M. Calandra, R. Car, C. Cavazzoni, D. Ceresoli, G. L. Chiarotti, M. Cococcioni, I. Dabo, A. Dal Corso, S. de Gironcoli, S. Fabris, G. Fratesi, R. Gebauer, U. Gerstmann, C. Gougoussis, A. Kokalj, M. Lazzeri, L. Martin-Samos, N. Marzari, F. Mauri, R. Mazzarello, S. Paolini, A. Pasquarello, L. Paulatto, C. Sbraccia, S. Scandolo, G. Sclauzero, A. P. Seitsonen, A. Smogunov, P. Umari, and R. M. Wentzcovitch. Quantum espresso: a modular and open-source software project for quantum simulations of materials. *Journal of Physics: Condensed Matter*, 21(39):395502, 2009.

[78] R. Mittal, L. Pintschovius, D. Lamago, R. Heid, K-P. Bohnen, D. Reznik, S. L. Chaplot, Y. Su, N. Kumar, S. K. Dhar, A. Thamizhavel, and Th. Brueckel. Measurement of anomalous phonon dispersion of $CaFe_2As_2$ single crystals using inelastic neutron scattering. *Phys. Rev. Lett.*, 102:217001, May 2009.

[79] R. Mittal, R. Heid, A. Bosak, T. R. Forrest, S. L. Chaplot, D. Lamago, D. Reznik, K.-P. Bohnen, Y. Su, N. Kumar, S. K. Dhar, A. Thamizhavel, Ch. Rüegg, M. Krisch, D. F. McMorrow, Th. Brueckel, and L. Pintschovius. Pressure dependence of phonon modes across the tetragonal to collapsed-tetragonal phase transition in $cafe_2as_2$. *Phys. Rev. B*, 81:144502, Apr 2010.

[80] We used the pseudopotentials La.pbe-nsp-van.UPF, Fe.pbe-paw_kj.UPF, As.pbe-n-van.UPF and O.pbe-van_ak.UPF from the http://www.quantum-espresso.org distribution.

[81] D. J. Singh and M.-H. Du. Density functional study of $LaFeAsO_{1-x}F_x$: A low carrier density superconductor near itinerant magnetism. *Phys. Rev. Lett.*, 100:237003, Jun 2008.

[82] J. Zhao, Q. Huang, C. de La Cruz, S. Li, J. W. Lynn, Y. Chen, M. A. Green, G. F. Chen, G. Li, Z. Li, J. L. Luo, N. L. Wang, and P. Dai. Structural and magnetic phase diagram of $CeFeAsO_{1-x}F_x$ and its relation to high-temperature superconductivity. *Nature Materials*, 7:953–959, December 2008.

[83] R. Veness, D. Ramos, P. Lepeule, A. Rossi, G. Schneider, and S. Blanchard. Installation and commissioning of vacuum systems for the lhc particle detectors. oai:cds.cern.ch:1199583. (CERN-ATS-2009-005):4 p, Jul 2009.

[84] R. E. H. Clark and D. Reiter. *Nuclear Fusion Research: Understanding Plasma-surface Interactions*. Springer, 2005.

[85] D. A. Young. *Phase Diagrams of the Elements*. University of California Press, 1991.

[86] P. K. Lam, M. Y. Chou, and M. L. Cohen. Temperature- and pressure-induced crystal phase transitions in Be. *Journal of Physics C: Solid State Physics*, 17(12):2065, 1984.

[87] L. X. Benedict, T. Ogitsu, A. Trave, C. J. Wu, P. A. Sterne, and E. Schwegler. Calculations of high-pressure properties of beryllium: Construction of a multiphase equation of state. *Phys. Rev. B*, 79:064106, Feb 2009.

[88] G. Robert, P. Legrand, and S. Bernard. Multiphase equation of state and elastic moduli of solid beryllium from first principles. *Phys. Rev. B*, 82:104118, Sep 2010.

[89] K. Nakano, Y. Akahama, and H. Kawamura. X-ray diffraction study of Be to megabar pressure. *Journal of Physics: Condensed Matter*, 14(44):10569, 2002.

[90] W. J. Evans, M. J. Lipp, H. Cynn, C. S. Yoo, M. Somayazulu, D. Häusermann, G. Shen, and V. Prakapenka. X-ray diffraction and raman studies of beryllium: Static and elastic properties at high pressures. *Phys. Rev. B*, 72:094113, Sep 2005.

[91] P. Souvatzis and O. Eriksson. Ab initio calculations of the phonon spectra and the thermal expansion coefficients of the $4d$ metals. *Phys. Rev. B*, 77(2):024110, Jan 2008.

[92] A. Sommerfeld and N. H. Frank. The statistical theory of thermoelectric, galvano- and thermomagnetic phenomena in metals. *Rev. Mod. Phys.*, 3:1–42, Jan 1931.

[93] D. C. Wallace. *Thermodynamics of Crystals*. John Wiley and Sons, Inc., 1972.

[94] G. Kresse and J. Hafner. Ab initio molecular dynamics for liquid metals. *Phys. Rev. B*, 47:558, 1993.

[95] G. Kresse and J. Hafner. Ab initio molecular-dynamics simulation of the liquid-metal-amorphous-semiconductor transition in germanium. *Phys. Rev. B*, 49:14251, 1994.

[96] G. Kresse and J. Furthmüller. Efficiency of ab-initio total energy calculations for metals and semiconductors using a plane-wave basis set. *Comput. Mat. Sci.*, 6:15, 1996.

[97] G. Kresse and J. Furthmüller. Efficient iterative schemes for ab initio total-energy calculations using a plane-wave basis set. *Phys. Rev. B*, 54:11169, 1996.

[98] P. E. Blöchl. Projector augmented-wave method. *Phys. Rev. B*, 50:17953, 1994.

[99] G. Kresse and D. Joubert. From ultrasoft pseudopotentials to the projector augmented-wave method. *Phys. Rev. B*, 59:1758, 1999.

[100] J. P. Perdew, K. Burke, and M. Ernzerhof. Generalized gradient approximation made simple. *Phys. Rev. Lett.*, 77:3865, 1996.

[101] J. P. Perdew, K. Burke, and M. Ernzerhof. Erratum: Generalized gradient approximation made simple. *Phys. Rev. Lett.*, 78:1396, 1997.

[102] H. Kleykamp. Thermal properties of beryllium. *Thermochimica Acta*, 345(2):179 – 184, 2000.

[103] A. Migliori, H. Ledbetter, D. J. Thoma, and T. W. Darling. Beryllium's monocrystal and polycrystal elastic constants. *Journal of Applied Physics*, 95(5):2436–2440, 2004.

[104] J. F. Smith and C. L. Arbogast. Elastic constants of single crystal beryllium. *Journal of Applied Physics*, 31(1):99–102, 1960.

[105] L. Gold. Evaluation of the stiffness coefficients for beryllium from ultrasonic measurements in polycrystalline and single crystal specimens. *Phys. Rev.*, 77:390–395, Feb 1950.

[106] E. Fisher and D. Dever. *Argonne National Laboratory Report*, 7155:192–197, 1965.

[107] D. J. Silversmith and B. L. Averbach. Pressure dependence of the elastic constants of beryllium and beryllium-copper alloys. *Phys. Rev. B*, 1:567–571, Jan 1970.

[108] L. R. Testardi and J. H. Condon. Landau quantum oscillations of the velocity of sound in Be: The strain dependence of the fermi surface. *Phys. Rev. B*, 1:3928–3942, May 1970.

[109] Y. Chen. First-principles study of phonon anomalies and the bcc-hcp martensitic phase transition. Master's thesis, Iowa State University, 1986.

[110] P. Souvatzis, S. Arapan, O. Eriksson, and M. I. Katsnelson. Temperature-driven -to-phase transformation in Ti, Zr and Hf from first-principles theory combined with lattice dynamics. *EPL (Europhysics Letters)*, 96(6):66006, 2011.

[111] P. Souvatzis, O. Eriksson, M. I. Katsnelson, and S. P. Rudin. Entropy driven stabilization of energetically unstable crystal structures explained from first principles theory. *Phys. Rev. Lett.*, 100(9):095901, Mar 2008.

[112] P. Souvatzis, D. Legut, O. Eriksson, and M. I. Katsnelson. *Ab initio* study of interacting lattice vibrations and stabilization of the β phase in Ni-Ti shape-memory alloy. *Phys. Rev. B*, 81:092201, Mar 2010.

[113] P. Souvatzis and S. P. Rudin. Dynamical stabilization of cubic ZrO_2 by phonon-phonon interactions: *Ab initio* calculations. *Phys. Rev. B*, 78:184304, Nov 2008.

[114] W. Luo, B. Johansson, O. Eriksson, S. Arapan, P. Souvatzis, M. I. Katsnelson, and R. Ahuja. Dynamical stability of body center cubic iron at the earths core conditions. *Proceedings of the National Academy of Sciences*, 2010.

[115] P. Souvatzis, O. Eriksson, M.I. Katsnelson, and S.P. Rudin. The self-consistent ab initio lattice dynamical method. *Computational Materials Science*, 44(3):888 – 894, 2009.

[116] G. Grimvall. *Thermophysical Properties of Materials*, volume 18 of *Selected Topics in Solid State Physics*. North-Holland Physics Publishing, 1986.